Space Sci Rev (2007) 131: 41–84
DOI 10.1007/s11214-007-9263-6

The Geology of Mercury: The View Prior to the MESSENGER Mission

James W. Head · Clark R. Chapman · Deborah L. Domingue · S. Edward Hawkins, III · William E. McClintock · Scott L. Murchie · Louise M. Prockter · Mark S. Robinson · Robert G. Strom · Thomas R. Watters

Received: 9 January 2007 / Accepted: 10 August 2007 / Published online: 10 October 2007

Abstract Mariner 10 and Earth-based observations have revealed Mercury, the innermost of the terrestrial planetary bodies, to be an exciting laboratory for the study of Solar System geological processes. Mercury is characterized by a lunar-like surface, a global magnetic field, and an interior dominated by an iron core having a radius at least three-quarters of the radius of the planet. The 45% of the surface imaged by Mariner 10 reveals some distinctive differences from the Moon, however, with major contractional fault scarps and huge expanses of moderate-albedo Cayley-like smooth plains of uncertain origin. Our current image coverage of Mercury is comparable to that of telescopic photographs of the Earth's Moon prior to the launch of Sputnik in 1957. We have no photographic images of one-half of the surface, the resolution of the images we do have is generally poor (∼1 km), and as with many lunar telescopic photographs, much of the available surface of Mercury is distorted by foreshortening due to viewing geometry, or poorly suited for geological analysis and

J.W. Head (✉)
Department of Geological Sciences, Brown University, Providence, RI 02912, USA
e-mail: James_Head@brown.edu

C.R. Chapman
Southwest Research Institute, 1050 Walnut St., Suite 400, Boulder, CO 80302, USA

D.L. Domingue · S.E. Hawkins, III · S.L. Murchie · L.M. Prockter
The Johns Hopkins University Applied Physics Laboratory, Laurel, MD 20723, USA

W.E. McClintock
Laboratory for Atmospheric and Space Physics, University of Colorado, Boulder, CO 80303, USA

M.S. Robinson
Department of Geological Sciences, Arizona State University, Tempe, AZ 85251, USA

R.G. Strom
Lunar and Planetary Laboratory, University of Arizona, Tucson, AZ 85721, USA

T.R. Watters
Center for Earth and Planetary Studies, National Air and Space Museum, Smithsonian Institution, Washington, DC 20560, USA

impact-crater counting for age determinations because of high-Sun illumination conditions. Currently available topographic information is also very limited. Nonetheless, Mercury is a geological laboratory that represents (1) a planet where the presence of a huge iron core may be due to impact stripping of the crust and upper mantle, or alternatively, where formation of a huge core may have resulted in a residual mantle and crust of potentially unusual composition and structure; (2) a planet with an internal chemical and mechanical structure that provides new insights into planetary thermal history and the relative roles of conduction and convection in planetary heat loss; (3) a one-tectonic-plate planet where constraints on major interior processes can be deduced from the geology of the global tectonic system; (4) a planet where volcanic resurfacing may not have played a significant role in planetary history and internally generated volcanic resurfacing may have ceased at ∼3.8 Ga; (5) a planet where impact craters can be used to disentangle the fundamental roles of gravity and mean impactor velocity in determining impact crater morphology and morphometry; (6) an environment where global impact crater counts can test fundamental concepts of the distribution of impactor populations in space and time; (7) an extreme environment in which highly radar-reflective polar deposits, much more extensive than those on the Moon, can be better understood; (8) an extreme environment in which the basic processes of space weathering can be further deduced; and (9) a potential end-member in terrestrial planetary body geological evolution in which the relationships of internal and surface evolution can be clearly assessed from both a tectonic and volcanic point of view. In the half-century since the launch of Sputnik, more than 30 spacecraft have been sent to the Moon, yet only now is a second spacecraft en route to Mercury. The MESSENGER mission will address key questions about the geologic evolution of Mercury; the depth and breadth of the MESSENGER data will permit the confident reconstruction of the geological history and thermal evolution of Mercury using new imaging, topography, chemistry, mineralogy, gravity, magnetic, and environmental data.

Keywords Mercury · MESSENGER · Planets and satellites: general · Mariner 10 · Caloris basin

1 Introduction and Background

In the 47 years between the launch of Sputnik, the first artificial satellite of the Earth, and the launch of the MErcury Surface, Space ENvironment, GEochemistry, and Ranging (MESSENGER) spacecraft to Mercury in 2004, the golden age of Solar System exploration has changed the terrestrial planets from largely astronomically perceived objects to intensely studied geological objects. During this transition, we have come to understand the basic range of processes differentiating planetary interiors, creating planetary crusts, and forming and modifying planetary surfaces. We have also learned how the relative importance of processes has changed with time; the chemical and mineralogic nature of surfaces and crusts; the broad mechanical and chemical structure of planetary interiors; and the relationship of surface geology to internal processes and thermal evolution (e.g., Head 2001a, 2001b). Together with these new insights have come outlines of the major themes in the evolution of the terrestrial planets (e.g., Head and Solomon 1981; Stevenson 2000).

These comprehensive advances and the synthesis of our understanding mask an underlying problem: Our level of knowledge of the terrestrial planets is extremely uneven, and this difference threatens the very core of our emerging understanding. Nothing better illustrates

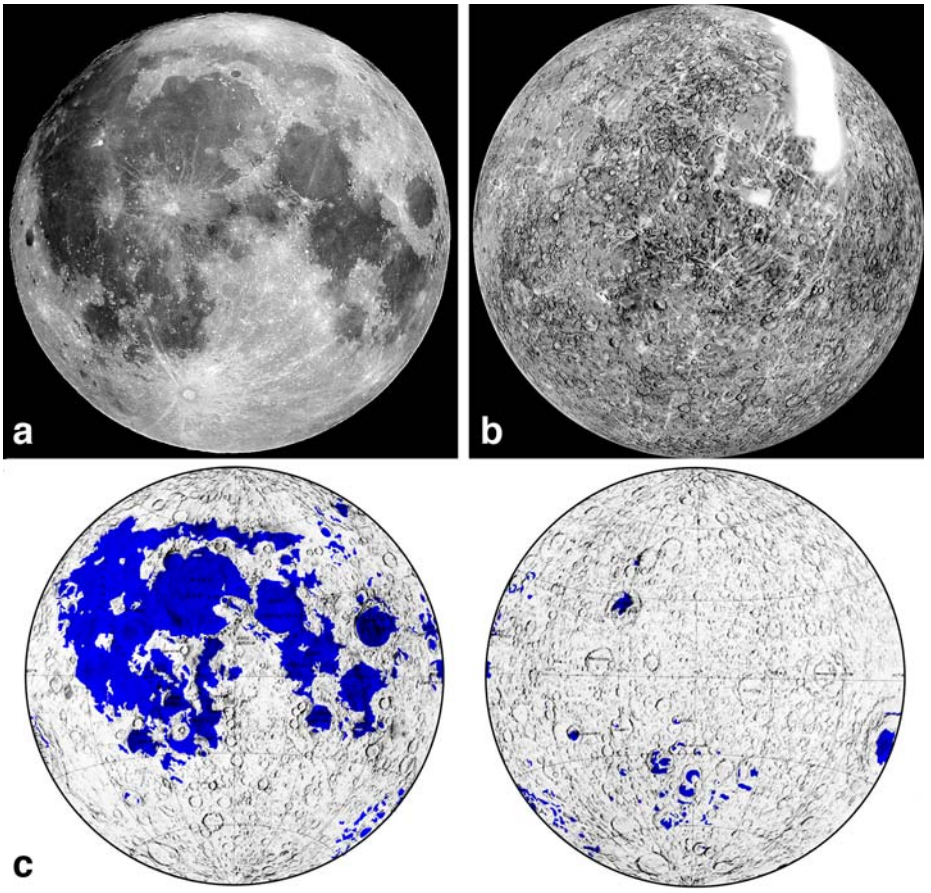

Fig. 1 (**a**) Earth-based telescopic photograph of the Moon typical of the area of the Moon seen prior to the time of the launch of Sputnik in 1957. Lick Observatory photograph. (**b**) Photographic coverage of Mercury from Mariner 10 (launched 1973) available at the time of the launch of the MESSENGER mission to Mercury in 2004, almost a half-century after Sputnik (shaded relief airbrush map; USGS, Flagstaff). (**c**) Map of the Earth's Moon in equal area projection showing the distribution of mare basalts on the nearside and farside. Compare with (**a**) and note the distinctive nearside-farside differences in lunar mare basalt distribution unknown before Luna 3 in 1959, and the general lack of mare deposits on the nearside limbs and southern nearside, a fact underappreciated due to Earth-based telescope viewing geometry (**a**)

this point than our currently poor knowledge of the planet Mercury. Mariner 10 imaged less than one-half of Mercury at a resolution of ∼1 km/pixel and even these data are variable in terms of quality due to differences in viewing geometry and solar illumination (Strom 1987). Indeed, our current image data for Mercury are generally comparable in resolution and coverage to our pre-Sputnik, Earth-based telescope photographs of the Moon (Fig. 1). However, the pre-Sputnik Earth-based telescope photographs of the Moon are actually more useful in terms of the range of different illumination conditions available. Recently, radar delay-Doppler mapping has begun to provide data with sufficient spatial resolution to enable some geologic studies of the side of Mercury not seen by Mariner 10 (e.g., Harmon et al. 2007).

Table 1 Instruments on the MESSENGER mission to Mercury (Gold et al. 2001; Santo et al. 2001)

Instrument	Description
Mercury Dual Imaging System (MDIS)	Wide-angle and narrow-angle imagers that map landforms and variations in surface spectra and gather topographic information (Hawkins III et al. 2007)
Gamma-Ray and Neutron Spectrometer (GRNS)	Maps the relative abundances of different elements and helps to determine if there is ice in the polar regions (Goldsten et al. 2007)
X-Ray Spectrometer (XRS)	Detects emitted X-rays to measure the abundances of various elements in the materials of the crust (Schlemm II et al. 2007)
Magnetometer (MAG)	Maps the magnetic field and any regions of magnetized rocks in the crust (Anderson et al. 2007)
Mercury Laser Altimeter (MLA)	Produces highly accurate measurements of topography (Cavanaugh et al. 2007)
Mercury Atmospheric and Surface Composition Spectrometer (MASCS)	Measures the abundances of atmospheric gases and minerals on the surface (McClintock and Lankton 2007)
Energetic Particle and Plasma Spectrometer (EPPS)	Measures the composition, distribution, and energy of charged particles (electrons and various ions) in magnetosphere (Andrews et al. 2007)
Radio Science (RS)	Measures very slight changes in spacecraft velocity to study interior mass distribution, including crustal thickness variations (Srinivasan et al. 2007)

Yet there are striking contradictions brought about by what little information we do have about Mercury. Could a terrestrial (Earth-like) planet form and evolve with no extrusive volcanic activity? Can the internally generated resurfacing of a terrestrial planet conclude at ∼3.8 Ga? Can one of the hottest planetary surfaces in the Solar System harbor an inventory of cometary ices? Can a planet containing an iron core proportionally much larger than that of the Earth not show demonstrable surface signs of internal convection? Can we confidently place Mercury in the scheme of geological and thermal evolution without ever having seen more than half of its surface with spacecraft observations? These and other questions formed the basis for the scientific rationale for the MESSENGER mission to Mercury (Solomon 2003). In this contribution, we review our basic current knowledge of the characteristics of the surface of Mercury at several scales, the geological features and processes observed thus far, and how this knowledge relates to its overall geological and thermal evolution. In the course of this review, we identify key unanswered questions, and how future studies and observations, in particular the MESSENGER mission and its instrument complement (Table 1), might address these. We first assess the state of knowledge of the surface from Earth-based remote sensing data, then review the current understanding of the geology of Mercury from Mariner 10 data, and end with a series of outstanding questions that can be addressed by the MESSENGER mission.

2 Remote Sensing and the Nature of the Surface of Mercury

Knowledge of the physical, chemical, mineralogic, and topographic properties of planetary surfaces is critical to understanding geological processes and evolution. Remote observations using instruments designed to characterize the surface at various wavelengths, first with Earth-based telescopes, and then with instruments on flybys and orbiters, have been the traditional manner in which we have learned about planetary surfaces. Two problems are presented by the proximity of Mercury to the Sun, first in making observations of a planet in such close solar proximity, and second the difficulty in placing a spacecraft in orbit around a planet so close to the huge solar gravity well. These factors, coupled with the apparent spectral blandness of Mercury, have resulted in rather limited knowledge of the nature of the optical surface. Here we review current knowledge and outstanding problems that can be addressed with MESSENGER instrument measurements and data.

2.1 Chemistry and Mineralogy

We know very little about the surface composition of Mercury (see detailed discussion in Boynton et al. 2007). Several decades ago it was realized that Mercury has a steeply reddened, quite linear reflectance spectrum throughout the visible and near-infrared (McCord and Clark 1979; Vilas 1988). It is similar to, but even redder than, the reddest lunar spectrum. Debate over the existence of minor spectral features in this spectral range (especially a possible pyroxene band near 0.95 μm) has been resolved in recent years by well-calibrated, higher quality spectra: Mercury's spectrum varies spatially from featureless to one with a shallow but well-resolved pyroxene absorption band (Fig. 2, bottom) (Warell et al. 2006). There are hints of absorption and emission features at longer infrared wavelengths (dominated by thermal emission) (Fig. 2, top), but their reality and the mineralogical implications have been debated (Vilas 1988; Boynton et al. 2007).

As is the case with the Moon, interpretation of such data by comparison with laboratory samples of plausible minerals is complicated by the major role played by space weathering (the modification of the inherent spectral signature of the minerals present by bombardment and modification of the minerals by micrometeorites, solar wind particles, etc.). Because Mercury is closer to the mineral-damaging radiation of the Sun, meteoroid impact velocities are much higher there, and Mercury's greater surface gravity inhibits widespread regolith ejecta dispersal, space weathering is predicted to be even more substantial than on the Moon, and it is likely that Mercury's spectrum is modified by space weathering even more than the lunar spectrum (e.g., Noble and Pieters 2003). Mineral grains at Mercury's optical surface are probably heavily shocked, coated with submicroscopic metallic iron, and otherwise damaged (e.g., Noble and Pieters 2003).

Although exogenous materials space-weather Mercury's surface, they are not expected to contaminate the mineralogical composition of the surface (by addition of exogenous material) to a degree that would generally be recognizable in remote-sensing data. The volumetric contribution of meteoritic material to lunar regolith samples is $\sim 1-2\%$ and there is no reason to expect it to be very different on Mercury. This is primarily because the projectile volume is tiny compared with the volume of planetary surface material that is displaced in a cratering event and cycled through the regolith. In addition, the Moon loses more mass than it gains by impact (Shuvalov and Artemieva 2006) and despite Mercury's higher escape velocity the greater impact velocities probably result in less retention of projectile material on Mercury. Darkening by admixture of fine carbonaceous material is probably overwhelmed by direct space-weathering effects. Small percentages of exogenous material are important

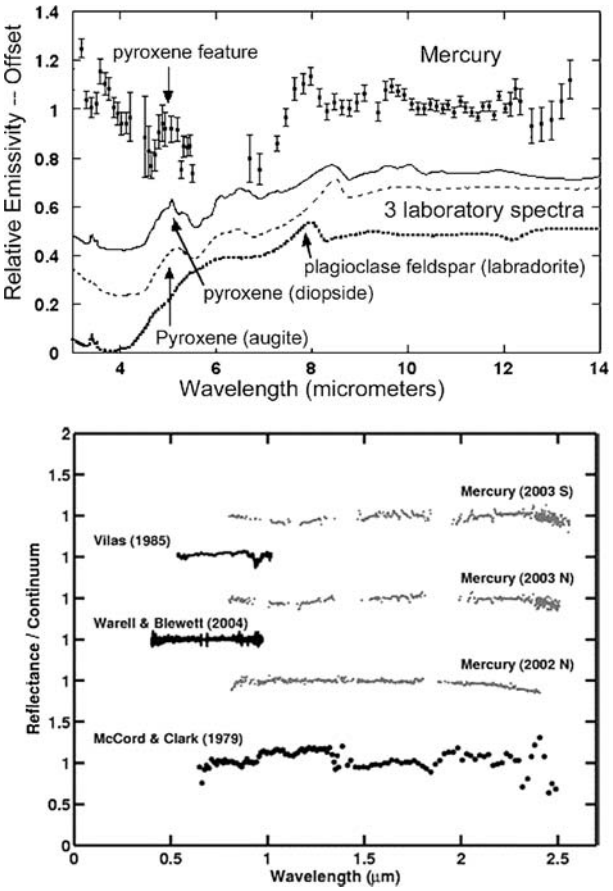

Fig. 2 Spectra of the surface of Mercury. (*Top*) A spectrum for the surface of Mercury in the mid-infrared (Sprague et al. 2002). Comparison with laboratory samples shows a peak near 5 μm that has been attributed to pyroxene and one near 8 μm similar to the spectral characteristics of anorthitic feldspar (Strom and Sprague 2003). (*Bottom*) Infrared Telescope Facility (IRTF) spectra from three different locations on Mercury (*gray*) compared with three other telescopic spectra (*black*). Solar reflectance and thermal emission components for the IRTF spectra have been removed, and each spectrum has been divided by a linear fit to the continuum. All spectra are normalized at 1 μm. The FeO absorption band is seen at 0.8–1.1 μm in the 2003N and 2003S spectra but absent in the 2002N spectrum, indicating lateral variability on the surface. From Warell et al. (2006)

to the degree that they are cold-trapped at the poles or visible in the tenuous atmosphere of Mercury.

A common interpretation of Mercury's nearly featureless spectrum is that its surface is analogous to the lunar anorthositic crust (Tyler et al. 1988; Sprague et al. 1994) (Fig. 2, bottom). But is there evidence for mare-like basalts that might have formed the smooth plains? Recent analyses have revealed the presence of a shallow 0.8–1.3 μm absorption feature centered near 1.1 μm that can be confidently interpreted as a characteristic iron-bearing silicate absorption (Fig. 2, bottom) (Warell et al. 2006), indicating that at least locally, soils may contain up to a few percent FeO. The scale of the observations precludes assignment of these spectra to specific geological units. Analysis of the exosphere of Mercury from ground-based observations has revealed enhanced Na and K emissions (e.g., Sprague et al. 1998) that may be correlated with specific areas on the surface of Mercury, specifically very fresh impact craters.

Ground-based remote sensing has also focused on imaging the parts of Mercury unimaged by Mariner 10 using advanced astronomical techniques (charge-coupled device, or CCD cameras and short exposure times) and modern processing software (combination of multiple images) (Warell and Limaye 2001; Mendillo et al. 2001; Ksanfomality 2004; Ksanfomality et al. 2005). Such efforts have resulted in the interpretation of a very large

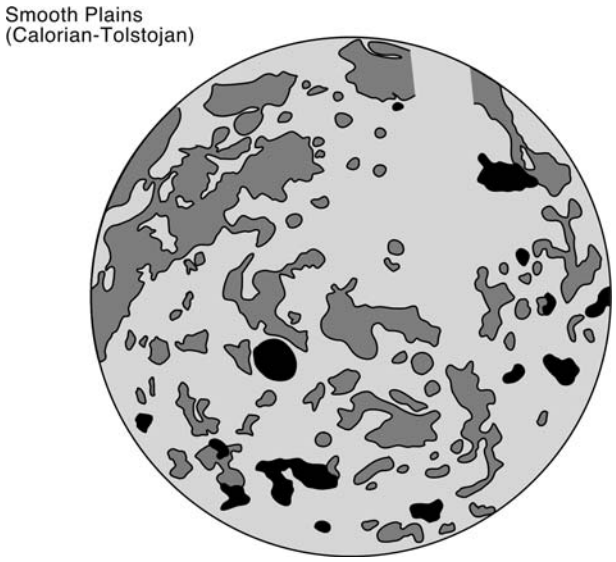

Fig. 3 Distribution of smooth plains on Mercury. Calorian-aged smooth plains are shown in dark gray, and Calorian and/or Tolstojan are shown in black. The remainder is cratered terrain. Together these smooth plains cover about 10.4×10^6 km^2 or 40% of the part of Mercury imaged by Mariner 10. Lambert equal-area projection centered on 0°N, 260°E (100°W), with north to the top. From Spudis and Guest (1988). Copyright, Arizona Board of Regents

impact basin (up to 2,300 km) with a dark central region in the unimaged part of Mercury (Ksanfomality 2004).

No totally self-consistent physical and chemical model for the composition, grain-sizes, and other parameters of Mercury surface soils has yet been devised that is fully compatible with these observations. Until space weathering processes are better understood, it will remain uncertain what firm constraints can be placed on Mercury's surface composition and its variation in relation to geologic units. The results from MESSENGER's numerous instrumental measurements (see also Boynton et al. 2007) (Table 1) will be critical to this understanding.

The Mariner 10 spacecraft carried no instrumentation capable of providing compositionally diagnostic remote-sensing information. The color images taken of Mercury have been reprocessed in recent years, showing slight but real differences in color, which may be correlated with surface morphology (Robinson and Lucey 1997). It is not clear whether variations in titanium content of surface soils might be responsible for the observed variations, as they are for color variations within the lunar maria. Albedo variations may also reflect, in some unknown way, variable composition, but Mercury lacks albedo variations as prominent as those between the highlands and maria of the Moon.

Initial analyses of Manner 10 color images of Mercury led to three major conclusions: crater rays and ejecta blankets are bluer (higher ratio of ultraviolet, or UV, to orange) than average Mercury, color boundaries often do not correspond to photogeologic units, and no low-albedo blue materials are found that are analogous to titanium-rich lunar mare deposits (Hapke et al. 1980; Rava and Hapke 1987). From these early studies it was noted that in a few cases color boundaries might correspond to mapped smooth plains units (Fig. 3); for example, Tolstoj basin (Rava and Hapke 1987) and Petrarch crater (Kiefer and Murray 1987). However, the calibration employed in these earlier studies did not adequately remove vidicon blemishes and radiometric residuals. A recalibration of the Mariner 10 UV (375 nm) and orange (575 nm) images resulted in a significantly increased signal-to-noise ratio (Robinson and Lucey 1997). These improved images were mosaicked and have been interpreted to indicate that color units correspond to previously mapped smooth plains on Mercury, and further that some color units are the re-

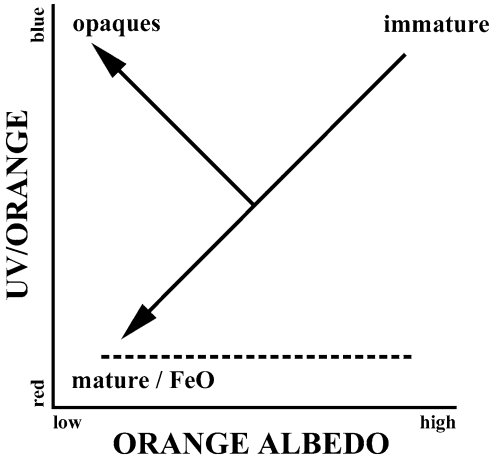

Fig. 4 Trends in the visible color of the lunar surface. The visible color of the lunar surface can be described by two perpendicular trends (opaque mineral concentration and iron-plus-maturity). The addition of ferrous iron to an iron-free silicate material (e.g., anorthosite) reddens the visible slope and lowers the albedo (a translation down the iron-maturity line; upper right to lower left). Color changes in lunar soil during maturation mimic the iron trend. As soils mature they redden (UV brightness/orange brightness) and their albedo decreases (orange brightness); soils translate down the iron-maturity line from upper right to lower left as they age. Adding spectrally neutral opaque minerals, such as ilmenite, results in a color trend that is nearly perpendicular to the iron-maturity line. Opaques lower the albedo but decrease the relative redness (an increase in the UV/orange ratio) of lunar soils. These two trends can be used to map the distribution of opaques (opaque index) and the iron-plus-maturity parameter through a coordinate rotation such that their perpendicular axes become parallel with the *X* and *Y* axes of the color-albedo plot (Robinson and Lucey 1997; Lucey et al. 1998); the *dotted line* indicates the position of the iron-maturity line after rotation. Adapted from Robinson and Lucey (1997)

sult of compositional heterogeneities in the crust of Mercury (Robinson and Lucey 1997; Robinson and Taylor 2001).

The newly calibrated Mariner 10 color data were interpreted in terms of the color reflectance paradigm that ferrous iron lowers the albedo and reddens (relative decrease in the UV/visible ratio) soil on the Moon and Mercury (Hapke et al. 1980; Rava and Hapke 1987; Cintala 1992; Lucey et al. 1995, 1998). Soil maturation through exposure to the space environment has a similar effect; soils darken and redden with the addition of submicroscopic iron metal and glass (Fig. 4). In contrast, addition of spectrally neutral opaque minerals (i.e., ilmenite) results in a trend that is nearly perpendicular to that of iron and maturity: Opaque minerals lower the albedo and increase the UV/visible ratio (Hapke et al. 1980; Rava and Hapke 1987; Lucey et al. 1998). For the Moon, the orthogonal effects of opaques and iron-plus-maturity are readily seen by plotting visible color ratio against reflectance (Lucey et al. 1998).

From Mariner 10 UV and orange mosaics a similar plot was constructed for the Mercury observations, and a coordinate rotation resulted in the separation of the two perpendicular trends (opaque mineral abundance from iron-plus-maturity) into two separate images (Robinson and Lucey 1997). The rotated data made possible the construction of two parameter maps: one delineating opaque mineralogy and the other showing variations in iron and maturity (Figs. 5 and 6). The opaque parameter map distinguishes units corresponding to previously mapped smooth plains deposits. The three best examples are the plains associated with Rudaki crater, Tolstoj basin, and Degas crater, each distinguished by their low

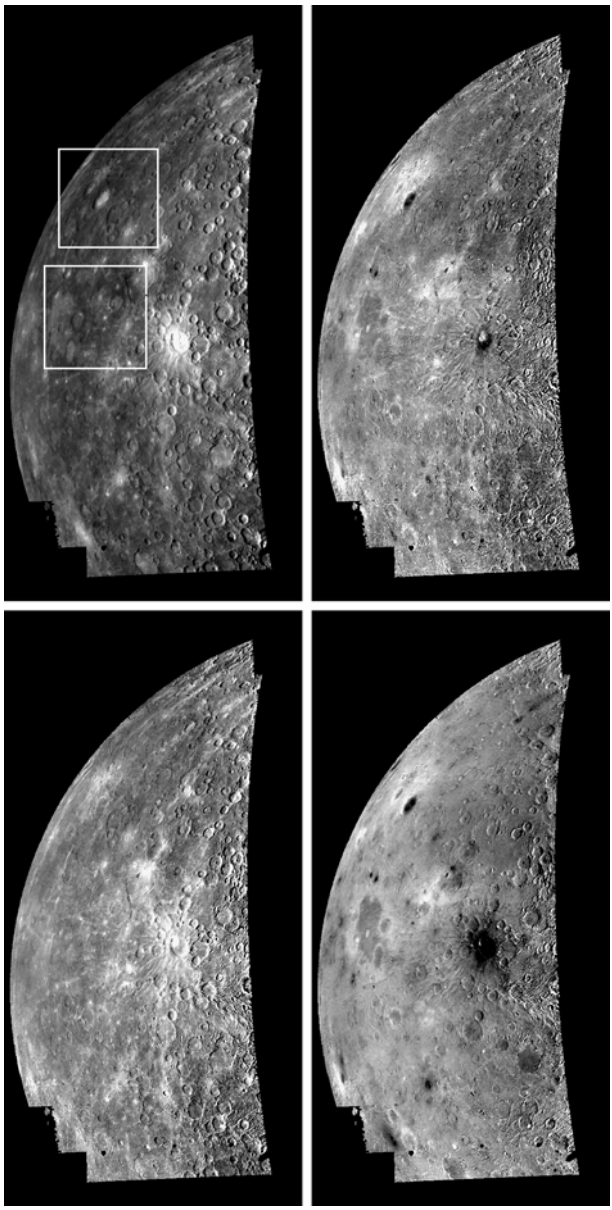

Fig. 5 Essential spectral parameters for the Mariner 10 incoming hemisphere. (*Upper left*) Orange (575 nm) albedo; boxes indicate areas enlarged in Fig. 6 (top is B, bottom is A). (*Upper right*) Relative color (UV/orange); higher tones indicate increasing blueness. (*Lower left*) Parameter 1-iron-maturity parameter; brighter tones indicate decreasing maturity and/or decreasing FeO content. (*Lower right*) Parameter 2-opaque index; brighter tones indicate increasing opaque mineral content. The relatively bright feature in the center right of the albedo image is the Kuiper-Muraski crater complex centered at 12°S, 330°E (30°W). Adapted from Robinson and Lucey (1997)

opaque index relative to their corresponding basement materials (Robinson and Lucey 1997; Robinson et al. 1997, 1998). In all three cases, the basement material is enriched in opaques.

A critical observation is that none of these units show a distinct unit boundary in the iron-plus-maturity image that corresponds to the morphologic plains boundary, leading to the interpretation that the smooth plains have an iron content that differs little from the global average. In the case of the Tolstoj basin (Robinson et al. 1998), a distinct mappable opaque index unit corresponds with the asymmetric NE–SW trending ejecta pattern of the basin, known as the Goya Formation (Schaber and McCauley 1980; Spudis and Guest 1988).

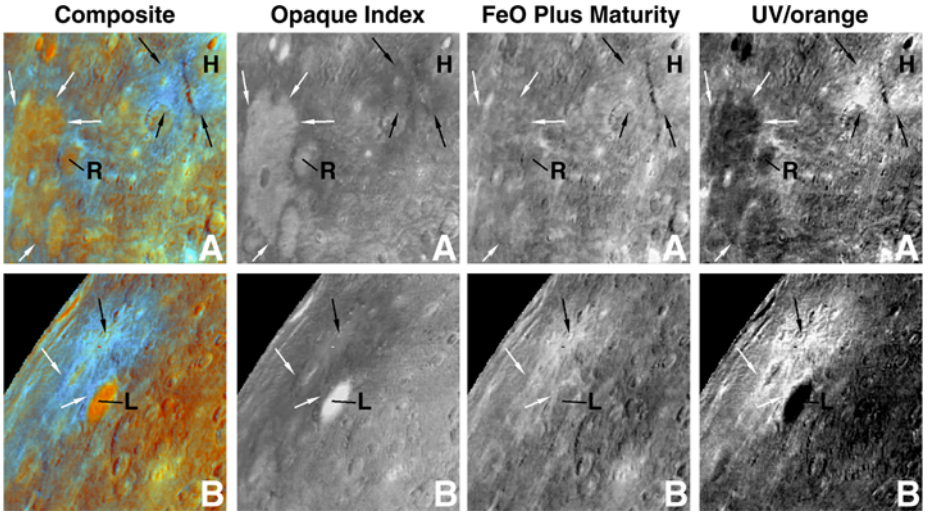

Fig. 6 Color ratio images of portions of Mercury. Enlargement of areas found on the Mariner 10 incoming hemisphere, keying on color units indicative of possible volcanically emplaced materials near the crater Rudaki (*R*; 120 km diameter; *top row*, *A*), Homer (*H*; 320 km diameter; *top row*, *A*), and Lermontov (*L*; 160 km diameter; *bottom row*, *B*). *Red* is formed from the inverse of the opaque index (increasing redness indicates decreasing opaque mineralogy; Fig. 5, lower right), the green component is the iron-maturity parameter (Fig. 5, lower left), and blue shows the relative color (UV/orange ratio; Fig. 5, upper right). The plains unit seen west and south and filling the crater Rudaki exhibits embaying boundaries indicative of material emplaced as a flow, and it has a distinct color signature relative to its surroundings. The blue material on the southwest margin of the crater Homer exhibits diffuse boundaries, is insensitive to local topographic undulations (*black arrows*), and is aligned along a linear segment of a Homer basin ring. A portion of the blue material seen northwest of the crater Lermontov is somewhat concentric to a small impact crater (*black arrow*) and may represent material excavated from below during the impact. However, examination of the iron-maturity parameter and opaque index images (*bottom row*) suggests that the darkest and bluest material (*white arrows*) in the deposit is not associated with an impact ejecta pattern, but rather that the anomalous lighter blue ejecta is composed of the dark material, although less mature and possibly with an admixture of basement material, overlying the darker blue portions of the deposit. Note that the opaque index was inverted relative to that shown in Fig. 5 to enhance contrast in the color composites (upper left and lower left panels). Adapted from Robinson and Lucey (1997)

This stratigraphic relation implies that formation of the Tolstoj basin (~550 km diameter) resulted in excavation of anomalously opaque-rich material from within the crust. The Goya Formation is not a mappable unit in the iron-plus-maturity image, indicating that its FeO content does not differ significantly from the local (and hemispheric) average.

A distinctive unit exhibiting diffuse boundaries (Fig. 6) is found near both Homer and Lermontov craters; examination of the iron-maturity parameter and opaque index images reveals that the darkest and bluest material in this deposit is not associated with an ejecta pattern, leading Robinson and Lucey (1997) to favor a pyroclastic origin (Figs. 6 and 7). The relatively blue color, high opaque index, and low albedo of these materials (for both areas) are consistent with a more mafic material, possibly analogous to a basaltic or gabbroic composition, or simply an addition of opaque minerals. Sprague et al. (1994) reported a tentative identification of basalt-like material in this hemisphere with Earth-based thermal IR measurements, while later microwave measurements were interpreted to indicate a total lack of areally significant basaltic materials on Mercury (Jeanloz et al. 1995). Earth-based spectral measurements have often been unable to resolve a ferrous iron band or to make any unassailable compositional infer-

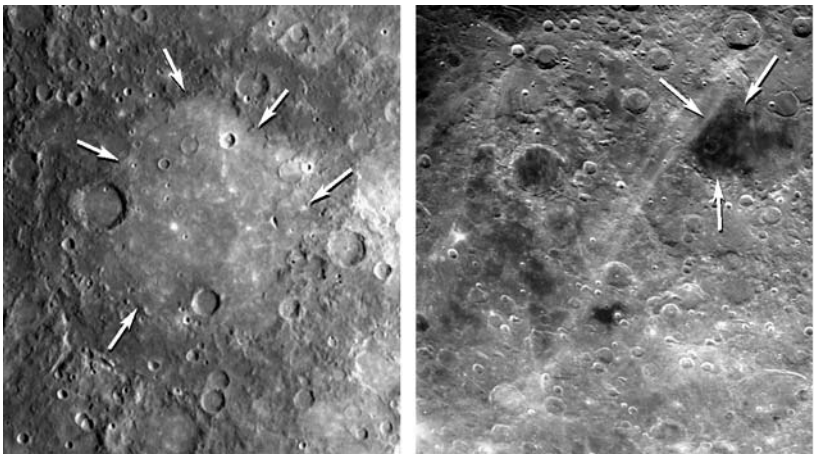

Fig. 7 A visual comparison of plains interpreted by some as flood lavas on Mercury found on the floor of the Tolstoj basin [*left*, 17°S, 196°E (164°W)] with Mare Humboldtianum on the Moon (*right*, 56°N, 280°E). Both data sets were acquired by Mariner 10 with similar resolutions (∼1 km per pixel; each image is about 625 km across) and viewing geometries (incidence angle = 65° for Mercury; 55° for the Moon). The most obvious distinguishing characteristic of the lunar mare deposit is its albedo contrast with the underlying highlands (*right*), a contrast not observed for Mercury (*left*). The key morphologic properties used to identify flood lavas on the Moon (other than albedo) are embayment relationships and ponding in topographic lows (usually basins; see *arrows* on both images). For the Moon, classic flow features such as flow fronts and vents are not visible at a scale of 1 km, except in some cases under low-Sun illumination (see Milkovich et al. 2002, and references therein)

ences (Vilas 1988), although a generally anorthositic crust is favored (Blewett et al. 2002; Warell and Blewett 2004). From the data currently available it is not possible to identify basaltic material or of any other rock type; however, the Mariner 10-derived spectral parameters, stratigraphic relations, and morphology are interpreted by numerous workers to be consistent with volcanically emplaced materials (e.g., Spudis and Guest 1988; Robinson and Lucey 1997). The areal extent of these diffuse deposits is small, and thus it is unlikely that current Earth-based observation could detect their presence. Regardless of the mode of emplacement, the materials found around the craters Homer and Lermontov, and the plains units identified earlier (Figs. 5–7), argue that significant compositional units occur within the crust of Mercury and that at least some of them were likely to have been emplaced by volcanic processes.

Thus, Mariner 10 data provide clues to the nature and distribution of spectrally distinctive parts of the crust of Mercury related to processes of crustal differentiation, impact excavation, maturation, plains relationships, and possible pyroclastic volcanism. MESSENGER (Table 1) will provide high-resolution multispectral images of much of the surface of Mercury that, together with the results of high-spectral-resolution data, will permit characterization of the mineralogy of the surface. Together with data on crustal chemistry (e.g., Boynton et al. 2007), MESSENGER will thus provide a more global characterization of the chemistry and mineralogy of the crust, and the documentation of variations in a host of geological environments. For example, analysis of the ejecta deposits and central peaks of craters with a range of diameters can provide essential information on the crustal structure of Mercury, as has been done on the Moon (e.g., Tompkins and Pieters 1999), and examination of the range of mineralogy of the plains can lead to important insight into the origin and source hetero-

geneity of volcanically emplaced plains, as has been done on the Moon (e.g., Hiesinger et al. 2003).

2.2 Physical Properties: Photometry

The physical properties of the regolith on Mercury (such as porosity, particle size distribution, surface roughness, and particle albedo and structure) can be constrained through the analysis and modeling of photometric observations. To date these photometrically derived properties for Mercury have been studied through the analysis of both telescopic observations (Danjon 1949; de Vaucouleurs 1964; Dollfus and Auriere 1974; Mallama et al. 2002; Warell and Limaye 2001) and Mariner 10 spacecraft measurements (Hapke 1984; Bowell et al. 1989; Robinson and Lucey 1997). There have been several studies of Mercury's photometric properties using Hapke's (1993) model (Veverka et al. 1988; Domingue et al. 1997; Mallama et al. 2002; Warell 2004), especially in comparison to similar studies of the Moon (Veverka et al. 1988; Mallama et al. 2002; Warell 2004). Early modeling of Mercury's photometric phase curve using this model was performed by fitting Danjon's (1949) disk-integrated observations and comparing the resulting fits to disk-resolved measurements taken from Mariner 10 images (Veverka et al. 1988; Domingue et al. 1997). Danjon's data set covers 3° to 123° phase angle, which does not adequately constrain the opposition surge (in terms of detecting any coherent backscatter effects, thus poorly constraining regolith porosity and particle size distribution) or the backscattering regime (phase angles beyond 120°, which constrain surface roughness versus albedo and particle structure). More recent observations by Mallama et al. (2002) extended the phase angle coverage range (2° to 170°), especially in the backscattering regime. In addition, disk-resolved photometric measurements are now available from high-resolution CCD images obtained with the Swedish Vacuum Solar Telescope (SVST; Warell and Limaye 2001). Warell (2004) improved previous modeling efforts by simultaneously fitting both disk-integrated (Mallama et al. 2002) and disk-resolved (Warell and Limaye 2001) observations, using a more comprehensive Hapke model (Hapke 1981, 1984, 1986, 1993, 2002) and a Henyey–Greenstein single particle scattering function (which can be compared with the laboratory studies of particle scattering behavior versus particle structure by McGuire and Hapke 1995).

The photometric studies of Veverka et al. (1988), based on analysis of disk-integrated data from Danjon (1949), found that in comparing the regoliths on the Moon and Mercury, Mercury's regolith was less backscattering, possibly more compact, and similar in surface roughness. Similar modeling by Mallama et al. (2002) of their disk-integrated observations found that, in comparison, the regoliths of these two objects are similar in compaction and particle size distribution, and that the surface of Mercury is smoother. The results from Warell's (2004) simultaneous modeling of the disk-integrated and disk-resolved photometric observations are more in line with the results from Mallama et al. (2002). Compared with the lunar regolith, Warell (2004) showed that Mercury's surface has a slightly lower single scattering albedo, similar porosity, a smoother surface, and a stronger backscattering anisotropy in the single-particle scattering function. The larger range in phase angle coverage of the Mallama et al. (2002) data, modeled by both Mallama et al. (2002) and Warell (2004), provides a better determination of the surface roughness and particle scattering properties.

Porosity determinations based on Hapke's model are strongly coupled to assumptions made about the particle size distribution and the ratio of the radii of largest (r_{largest}) to smallest (r_{smallest}) particle within the regolith. The lunar regolith has been shown to have a grain-

size distribution, Y, given by

$$Y = \frac{\sqrt{3}}{\ln\left(r_{\text{largest}}/r_{\text{smallest}}\right)} \tag{1}$$

(Bhattacharya et al. 1975). If this particle size distribution is assumed to hold true for both the Moon and Mercury, then the relationship

$$h = -\left(\frac{3}{8}\right) Y \ln(\rho), \tag{2}$$

where h is the Hapke opposition width parameter and ρ is the porosity, can be used to estimate regolith porosity. Mallama et al. (2002) found an h value of 0.065 for Mercury, whereas Warell's (2004) preferred solutions for Mercury and the Moon gave h values of 0.09 and 0.11, respectively. For $r_{\text{largest}}/r_{\text{smallest}}$ ratio values from 100 to 10,000, the porosity difference between the surface of the Moon and Mercury is ~7%, with Mercury's regolith being slightly more porous (38% porosity with $r_{\text{largest}}/r_{\text{smallest}} = 1{,}000$).

Values for the Hapke surface roughness parameter vary between 20° and 25° (Veverka et al. 1988; Bowell et al. 1989; Domingue et al. 1997) to 8° to 16° (Mallama et al. 2002; Warell 2004). The disk-integrated observations of Mallama et al. (2002) and the disk-resolved observations of Warell and Limaye (2001) support a smoother surface on Mercury. However, the Mariner 10 disk-resolved data better match a surface with the higher, lunar-like roughness values. This discrepancy is most likely due to the variation in roughness across the surface of Mercury and the relative sampling of the surface by the different data sets (Warell 2004).

Analysis of the high-resolution CCD images of Mercury obtained with the SVST shows that there is an inverse relationship between the spectral slope and emission angle (Warell and Limaye 2001). A similar relationship between spectral slope and emission angle is observed for the Moon, but the relationship is more pronounced in the Mercury observations. Warell's (2002) interpretation is that the regolith of Mercury is more backscattering than the lunar regolith. The more backscattering nature of the surface is also seen in Warell's (2004) modeling of the integral phase curve and CCD images. When comparing the single particle scattering characteristics of the modeling solutions of the Moon and Mercury with the laboratory studies of McGuire and Hapke (1995), Warell (2004) found that the particles from both objects are characterized by grains with internal scatterers. The comparisons indicate that in general the regolith grains on Mercury have a higher number of internal scatterers and are more like the lunar mare materials than the lunar highlands. The backscattering nature of the grains on both the Moon and Mercury are commensurate with highly space-weathered, ground-up materials. The MESSENGER mission will provide important new information on the physical properties of the surface of Mercury from imaging observations at different viewing geometries, laser altimeter backscatter properties, albedo characterization of different geological environments, and the reflectance properties of surfaces of different ages.

2.3 Radar Observations

Earth-based radar observations from Arecibo and Goldstone have provided information on surface scattering properties, equatorial topography, deposits in permanently shadowed crater interiors, and preliminary information about the morphology and morphometry of portions of Mercury not observed by Mariner 10 (e.g., Harmon and Campbell 1988; Clark et al. 1988; Harmon and Slade 1992; Anderson et al. 1996; Harmon et al. 1986,

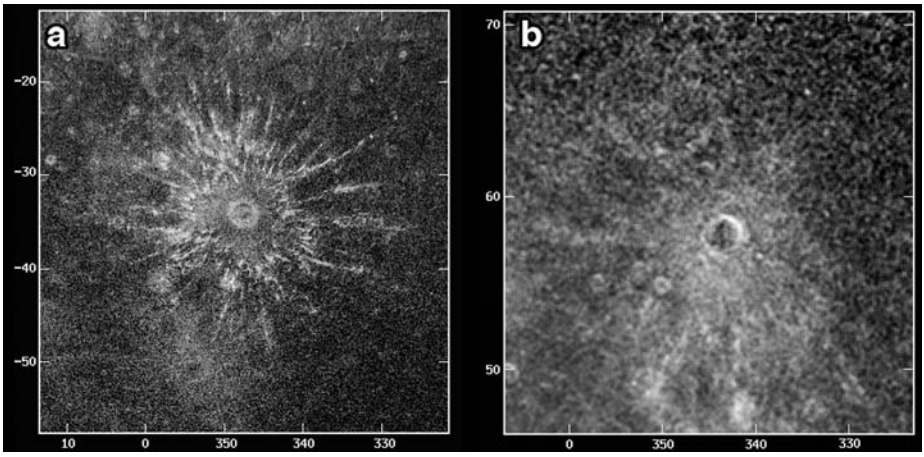

Fig. 8 Arecibo radar images from part of the surface not imaged by Mariner 10. (**a**) Feature "A," an 85-km-diameter crater whose radar ray system may be the most well-developed in the solar system (SC, same as transmitted sense polarization; i.e., same component transmitted and received). (**b**) Feature "B," a 95-km-diameter impact crater with a very bright halo but less distinct ray system. Feature "B," originally considered to be a candidate for a large volcanic edifice, is now clearly seen to be a very bright-haloed impact crater with a less distinct ray system than that of feature "A" (OC, opposite of transmitted sense polarization; i.e., opposite component received from that transmitted). Images from Harmon et al. (2007)

1994, 2001, 2007). Doppler spectrum shape and depolarization data yield information on dielectric properties and surface roughness, complementing the optical data. These data help confirm the presence of a regolith layer and show that the smooth plains are smooth at radar wavelengths (root mean square, or rms, slopes of about 4°). Quantitative data on equatorial topography have been very useful for the analysis of equatorial radius (~2,439.7 km) and shape, the range of altitudes (~7 km, from −2.4 to +4.6 km), and definition of the zero-altitude datum (+0.3 km), the most probable altitude as shown in the peak of the equatorial altimetric histogram (Harmon et al. 1986). Radar altimetry provided high-resolution topographic profiles for major features on Mercury (Harmon et al. 1986) showing a systematic difference in the depths of large craters between Mercury (shallower) and the Moon, and systematic differences between shadow measurements and radar measurements (17% lower) for large crater depths on Mercury. Other profiles documented the steep topography associated with major lobate fault systems (a 3 km drop in 70 km) and the rounded topography associated with arcuate scarps. Radar altimetry of basins and smooth plains shows the usefulness of depth determinations for basin degradation studies and regional topography for revealing large-scale undulations (downbowing) in the smooth plains. Altimetry of portions of Mercury not imaged by Mariner 10 revealed the extension of the circum-Caloris smooth plains into the unimaged hemisphere and suggested the presence of similar cratered terrain and plains there (Harmon et al. 1986).

Harmon et al. (2007) recently presented dual-polarization, delay-Doppler radar images of nonpolar and unimaged regions of Mercury obtained from several years of observations with the upgraded Arecibo S-band (12.6-cm) radar telescope. The images are dominated by radar-bright features associated with fresh impact craters. As previously reported, three of the most prominent crater features are located in the hemisphere not imaged by Mariner 10 and consist of feature "A", a crater 85 km in diameter whose radar ray system may be the most well-developed in the solar system (Fig. 8a), feature "B", a crater 95 km in diameter

with a very bright halo but less distinct ray system (Fig. 8b), and feature "C", with rays and secondary craters distributed asymmetrically about a 125-km-diameter source crater. Feature "B", originally considered to be a candidate for a large volcanic edifice (Harmon 1997), is now clearly seen to be a very bright-haloed impact crater with a less distinct ray system than that of feature "A" (compare Figs. 8a and 8b). Two excellent examples of large ejecta/ray systems preserved in an intermediate state of degradation were also described. Although no evidence for volcanic edifices or central sources of lava flows are reported by Harmon et al. (2007) in the unimaged portion of Mercury, diffuse radar albedo variations are seen that have no obvious association with impact ejecta. Some smooth plains regions such as the circum-Caloris plains in Tir, Budh, and Sobkou Planitiae and the interior of Tolstoj basin show high depolarized brightness relative to their surroundings, which is the reverse of the mare/highlands contrast seen in lunar radar images. In contrast, Caloris basin appears dark and featureless in the images. The high depolarized brightness of the smooth plains could be due to (1) compositional differences from the lunar maria (lower iron and titanium content and thus less electrically lossy than mare lavas); (2) rougher small-scale surface texture which, if the plains are volcanic, could be related to differences in lava rheology; (3) a different roughness state due to the relative youth of the surface; and/or (4) a higher dielectric constant (Harmon et al. 2007).

Thus, we anticipate that the MESSENGER mission image and altimeter data will provide important new insight into surface topography in terms of the statistics of crater depths, the documentation of large degraded basins, crater degradation processes, tectonics, plains emplacement, and a determination of the features and stratigraphic relationships necessary to reconstruct the geologic history of Mercury.

3 The Geology of Mercury: General Terrain Types, Stratigraphy, and Geologic Time Scale

Prior to Mariner 10 nothing was known about the geological features and terrain types on Mercury; this situation changed virtually overnight with the first Mariner 10 images and the two subsequent flybys (Murray 1975). Trask and Guest (1975) used traditional photogeologic methods and the Mariner 10 images covering about 45% of the planet to produce the first geologic terrain map of Mercury. They recognized (1) a widespread unit, intercrater plains, (2) heavily cratered plains, (3) the Caloris basin and related deposits, (4) smooth plains, (5) hilly and lineated terrain antipodal to the Caloris basin, and (6) numerous younger craters and their related deposits, drawing attention to the similarities in units and geological history of Mercury and the Moon.

Subsequent more detailed analyses of the images were undertaken in a comprehensive geological mapping program at a scale of 1 : 5 M (e.g., Schaber and McCauley 1980; De Hon et al. 1981; Guest and Greeley 1983; McGill and King 1983; Trask and Dzurisin 1984; Spudis and Prosser 1984; Grolier and Boyce 1984). These geological maps, together with specific studies assessing key geological processes (e.g., Gault et al. 1975; Strom et al. 1975; Pike 1988; Schultz 1988; Strom and Neukum 1988; Melosh and McKinnon 1988; Thomas et al. 1988), provided the basis for our current state of knowledge about the geological history of Mercury (e.g., Murray et al. 1975; Spudis and Guest 1988). A time-stratigraphic system for Mercury (e.g., Spudis 1985) based on the rock-stratigraphic classification constructed during the 1 : 5 M quadrangle mapping and the earlier definition and subdivision of the Caloris Group (McCauley et al. 1981), has facilitated a correlation of geological events over the hemisphere imaged by Mariner 10 (Spudis and Guest 1988, plate 1-6) (Fig. 9) and

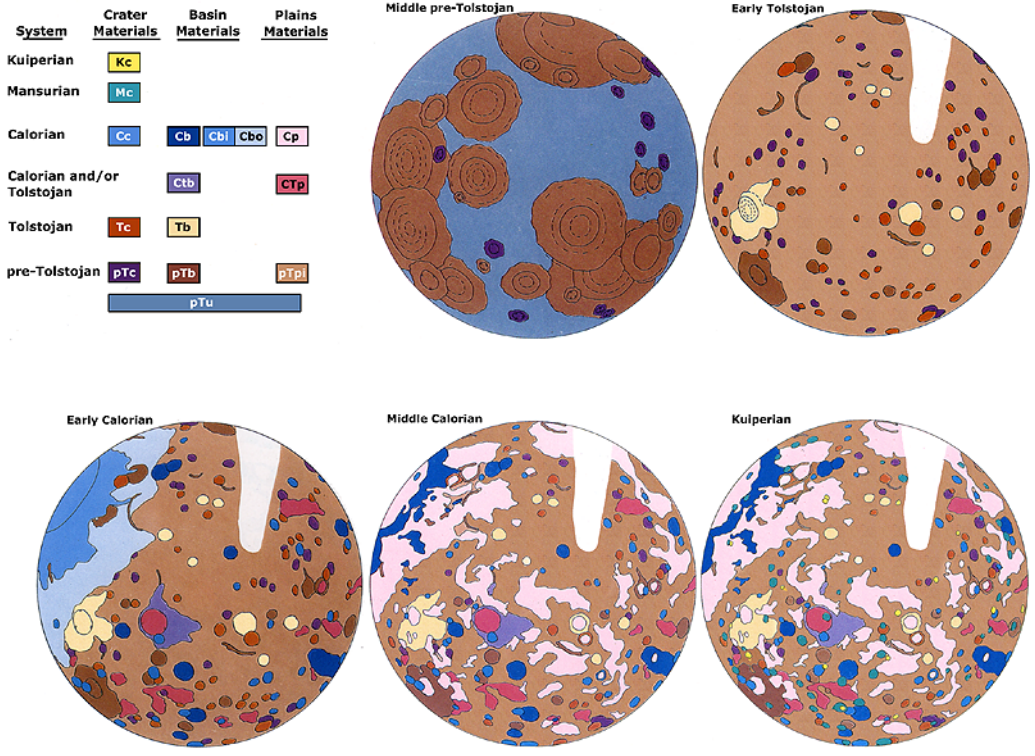

Fig. 9 Stratigraphic subdivisions of Mercury and a sequence of maps portraying the geologic setting at different times in the history of Mercury. After Spudis and Guest (1988). Copyright, Arizona Board of Regents

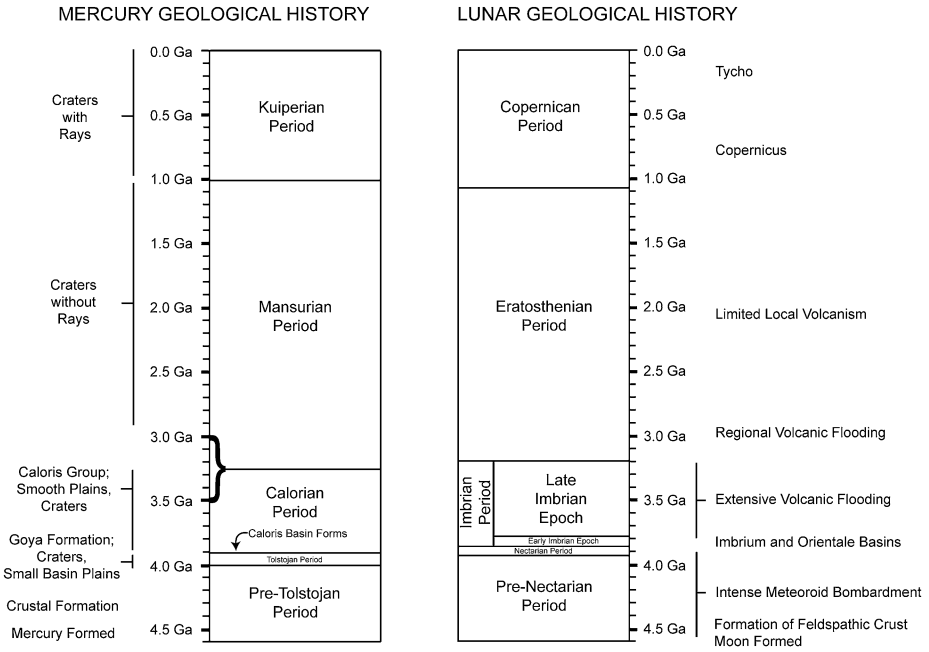

Fig. 10 The geological time scale of Mercury compared with that of the Moon. The absolute ages for Mercury are assumed to be tied to the lunar time scale but are not independently known. From Head (2006)

has permitted the continued comparison of the geological histories of Mercury and other planetary bodies begun soon after Mariner 10 (Murray et al. 1975).

Currently the geological history of Mercury is divided into five time-stratigraphic systems (Spudis and Guest 1988) (Figs. 9 and 10). The oldest predates the Tolstoj basin and consists largely of crater and multiringed basin deposits and extensive intercrater plains emplaced prior to the Tolstoj basin. Assuming that the heavily cratered terrains were produced by the same late heavy bombardment that is interpreted to have occurred on the Moon, this system is thought to predate 4.0 Ga and is approximately analogous to the pre-Nectarian on the Moon. This is also the very important period of crustal formation and early evolution during which time the impact rate was sufficiently high that the surface geological record was largely obliterated, and thus existing crater data are not very informative. For example, on Mars during this time, the crust formed, major crustal magnetic anomalies were emplaced, the fundamental global dichotomy in crustal thickness and topography was formed, and Tharsis, a major manifestation of internal thermal evolution, was emplaced (see Solomon et al. 2005). Despite our lack of knowledge of similar or analogous events in this period of the history of Mercury, MESSENGER and its instrument complement (Table 1) hold promise for detecting crustal magnetic anomalies, determining the origin of the magnetic field and assessing the properties of the outer core (Margot et al. 2007) and its implications for convection (e.g., Solomatov and Reese 2001), establishing the gravity field, determining global shape and topography, characterizing the elemental and mineralogical nature of the crust, establishing the major mode of crustal isostatic compensation (e.g., Zuber et al. 2007), and correlating all of these with the global geological context and history.

The base of the next youngest period, the Tolstojan System, is defined by the Tolstoj basin-forming event, and consists of Tolstoj and other crater and basin deposits as well as

plains materials. This is assumed to date from ~4.0 to 3.9 Ga and is equivalent to the Nectarian on the Moon. The base of the next overlying unit, the Calorian System, is defined by the Caloris basin-forming event (evidently the last major basin formed on Mercury, Fig. 10) and consists of Caloris basin deposits, smaller crater deposits and widespread smooth plains deposits. It is thought to extend from about 3.9 Ga to perhaps as young as 3.0–3.5 Ga and is analogous to the Imbrian Period on the Moon. The next youngest Mansurian Period is defined by the crater Mansur and consists of impact crater deposits that contain no bright rays (analogous to the Eratosthenian Period on the Moon). There is no evidence for regional volcanic or tectonic activity during this time in the portion of Mercury imaged by Mariner 10. The Mansurian is thought to span the period from the end of the Calorian to about 1 Ga, although the absolute chronology has not been determined to better than a factor of a few. The youngest Kuiperian Period is defined by the bright-rayed crater Kuiper; deposits consist of impact craters still maintaining their bright rays, and there is no evidence for any regional volcanic or tectonic activity. The Kuiperian extends from ~1.0 Ga to the present and is analogous to the Copernican Period on the Moon.

These five systems define a context for the occurrence of other geological activity (Fig. 10). Widespread contractional deformation during the Calorian Period, after the formation of the Caloris basin and the emplacement of Calorian smooth plains, resulted in the lobate scarp thrust faults and wrinkle ridges in the imaged hemisphere. This suggests that the compressional stresses that formed these tectonic landforms peaked after the end of the period of heavy bombardment (Watters et al. 2004). Long-wavelength folds may also have formed in the period of global contraction (e.g., Hauck et al. 2004). Smaller wrinkle ridges formed on the smooth plains, and their emplacement and deformation have been dated as later than the Caloris impact event but closely associated with Calorian time. Spudis and Guest (1988) marshaled evidence in favor of a volcanic origin for the smooth plains on Mercury, citing (1) their planet-wide distribution (Figs. 3 and 9), (2) their total volume well in excess of what could be explained by impact ejecta, and (3) crater density data that indicated that major expanses of circum-Caloris smooth plains substantially postdate Caloris and all other major basins (see their Table III). On the basis of these data, they concluded that although the evidence is indirect, it is compelling enough to conclude that Mercury underwent large-scale volcanic resurfacing subsequent to the Caloris basin-forming impact. The extent and duration of the Calorian Period, and thus of the emplacement of the smooth plains and their deformation by wrinkle ridges, is unknown. By analogy with the lunar maria, Spudis and Guest (1988) estimated its duration to be from about 3.9 Ga to perhaps as young as 3.0–3.5 Ga, but others have estimated that the duration is much shorter (e.g., Strom and Neukum 1988; Neukum et al. 2001; Strom et al. 2005). In the next section, we address the important question of impact cratering rates and the absolute time scale. It is clear, however, that the MESSENGER mission (Table 1) will obtain a significantly better understanding of the geological history of Mercury through acquisition of data showing the geology of the other half of its surface, data to obtain better crater size frequency distributions for age determinations, and topography to study geological and stratigraphic relationships.

4 Geological Processes on Mercury: Impact Cratering and Basin Formation

The Mariner 10 images offered the opportunity to study the impact cratering process in a planetary environment similar to the Moon in some ways (lack of an atmosphere and its effects during crater formation and modification), similar to Mars in others (gravity), and

different from both in terms of mean impact velocity. The morphology and morphometry of impact craters can provide significant insight into the physics of the cratering processes, as Mercury is a unique locale for calibrating the effects of impact velocity and gravity on a volatile-depleted silicate crust (e.g., Schultz 1988; Pike 1988). Thus, Mercury was viewed as a laboratory for the assessment of these variables and the Mariner 10 data as the first results. Analyses were undertaken to characterize the morphology and morphometry of fresh and degraded craters, and to assess the size-frequency distribution of impact craters to estimate ages of regional geological units defined by geological relationships and thus contribute to reconstruction of the geological history.

As with the Moon, Mars, Venus, and Earth, the morphologic complexity of impact craters (Fig. 11) was observed to increase systematically with diameter (Pike 1988). Key morphologic parameters were determined to be size dependent (e.g., depth, rim height, rim, floor and peak diameter; presence of bowl shape, flat floor, central peak, scalloped walls, wall terraces, etc.). Lunar-like classes of fresh craters were defined and ranged in increasing diameter from simple, to complex, to protobasin, to multiringed basin. The data permitted the relatively precise determination of transitions in depth/diameter relationships between the crater classes. The diameter of the transition from simple to complex craters on Mercury ($\sim$10.3 km) provided a comparison with that of the Moon, Mars, and Earth, and confirmed a strong inverse relationship with surface gravity and approach velocity. The new data showed that impact craters on Mercury and the Moon differed significantly in some other size-dependent aspects of crater form, such as protobasin, and two-ring basin, onset diameter. In a comprehensive review of crater and basin morphometry on the Earth, Mars, Moon, and Mercury, Pike (1988) found that neither average nor onset sizes of multiring basins on Mercury and the three other planets scale with gravity and concluded that surface gravity g, substrate rheology, and impactor velocity decrease in importance with increasing size of the impact, with g the last to disappear. Although much of the complexity of the interior of craters appears to be due to gravity-driven rim failure, inertially driven uplift of the crater bowl apparently played a major role in initiating the collapse. The apparent absence of clear influence of gravity on multiringed basin onset diameter led Pike (1988) to propose that multiringed basin formation is dominated by some combination of energy-scaled and hydrodynamic-periodic processes. Crater morphologic and morphometric characteristics were examined for craters on different substrates (e.g., smooth plains versus intercrater plains) in order to search for variations attributable to differences in the substrate physical properties. Although evidence for some variations was found, the effects were apparently minor.

MESSENGER data offer the opportunity to extend the study of crater morphometry globally, to increase the population and the statistical sample, to obtain more reliable quantitative measurements through altimeter observations and higher resolution images, and to search for substrate differences over larger areas.

The morphology of impact crater deposits added significant insight into the physics of the cratering process. For example, Gault et al. (1975) documented the role of gravity in the emplacement of ejecta relative to the Moon, illustrating the reduction in the range of the ballistic transport, the change in topography of the rim crest ejecta, and subsequent collapse and the formation of terraces. Furthermore, Schultz (1988) combined the Mercury observations with results from laboratory experiments and suggested that crater shapes intrinsically become flatter as the time for energy/momentum transfer increases, provided that a critical transfer time is exceeded. This resulted in the prediction that observed shallower craters on Mars relative to Mercury (at the same diameter) may be due to the low rms impact velocities at Mars relative to Mercury.

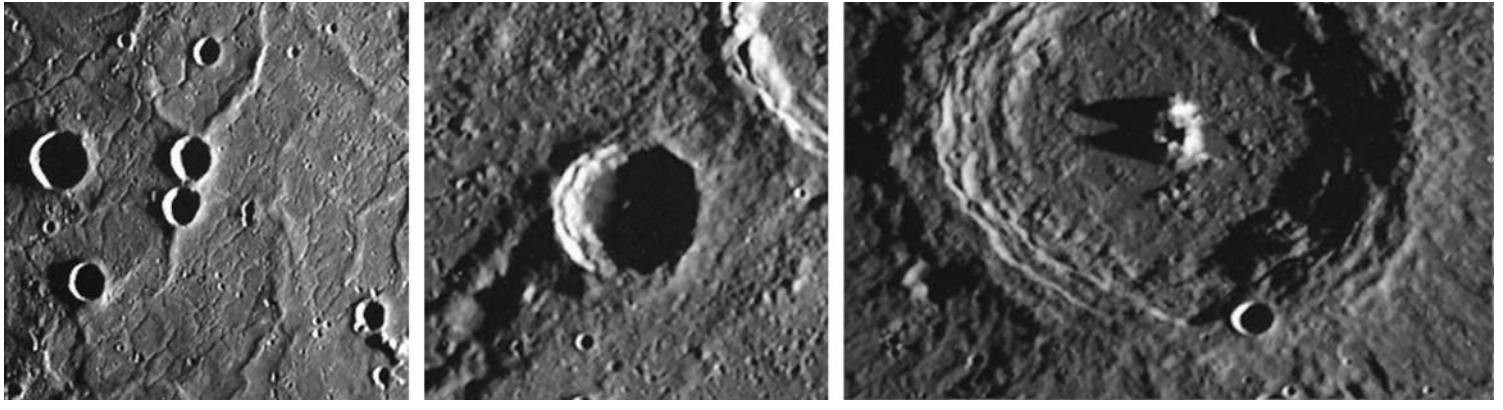

Fig. 11 Impact craters on Mercury revealed by Mariner 10. *Left*, a series of small circular, bowl-shaped simple craters less than ∼15 km in diameter (width of field is ∼175 km; Mariner 10 image 0000126). *Middle*, a crater in the diameter range 15–30 km, with a scalloped rim and the beginnings of wall slumping and flat floor, intermediate between simple and complex (width of field is 90 km; Mariner 10 image 0000098). *Right*, a large, complex crater greater than 30 km in diameter, with a polygonal outline, terraced walls, a flat floor, and a central peak (width of view is 110 km; Mariner 10 image 000080)

MESSENGER altimetry and imaging data, together with similar recently acquired data for Mars, will permit this prediction to be tested. Testing this hypothesis will permit the better understanding of potential differences in the impactor size-frequency distribution with time in different parts of the Solar System, a key parameter in assessing planetary chronology and interplanetary age comparisons (Schultz 1988). As pointed out by Schultz (1988), the cratering record on Mercury contains critical information for the true understanding of planetary bombardment history and distinguishing the effects of contrasting combinations of targets and impactors. Impact crater degradation processes on Mercury were also analyzed (e.g., Gault et al. 1975; Smith 1976) and shown to be very similar to the impact-caused degradation seen on the Moon (e.g., Head 1975) with important variations related to the more limited lateral ejecta dispersal on Mercury. MESSENGER image and altimetry data will provide the basis to quantify these degradation relationships and to assess the relative roles of impact degradation and viscous relaxation.

One of the most exciting discoveries of the Mariner 10 mission was the 1,300-km-diameter Caloris impact basin (Murray et al. 1974). This feature (Fig. 12), similar in morphology to lunar impact basins such as Orientale (e.g., McCauley 1977; McCauley et al. 1981), provided important insight into the nature of the surface of Mercury, the origin of circum-Caloris smooth plains (were they emplaced as impact ejecta, e.g., Wilhelms 1976a; or as volcanic plains, e.g., Trask and Strom 1976). The Caloris basin belongs to a class of features known as central peak and multiringed basins on the Moon (e.g., Wilhelms 1987) of which there are many more representatives on Mercury (e.g., Murray et al. 1974; Wood and Head 1976; Head 1978; McKinnon 1981; Pike and Spudis 1987; Pike 1988). Twenty central peak basins (protobasins) were identified from the Mariner 10 data (Pike 1988) with diameters between 72 and 165 km. Thirty-one two- ringed basins, between 132 and 310 km in diameter, and possibly as many as 23 multiringed basins, between 285 and 1,530 km, were also detected. Furthermore, many other, more degraded features may be basins poorly detected in the area imaged by Mariner 10. The degree of degradation and stratigraphic relationships of these large basins are a fundamental factor in the development of global stratigraphic relations on Mercury and other planets (e.g., Wilhelms 1987; Spudis and Guest 1988). Indeed, using Mariner 10 stereo image data, Watters et al. (2001) discovered a previously unknown impact basin. On the basis of the importance of high-resolution altimetry data in the detection of degraded craters and basins on Mars (e.g., Smith et al. 2001; Frey et al. 1999), it is obvious that the new MESSENGER image and stereo data, together with the altimeter data, will reveal many previously undetected basins in both the previously seen and unimaged areas of Mercury.

Related questions raised by the discovery of Caloris focus on how the interior of the planet might respond to such a huge event, both in the basin interior and its far exterior. For the far exterior, Mariner 10 discovered an unusual hilly and lineated terrain at the antipodal point of the Caloris basin. The hilly and lineated morphology disrupts crater rims and other pre-existing landforms, and stratigraphic relationships suggest that the texture formed at the same time as Caloris (Trask and Guest 1975; Spudis and Guest 1988). Similar terrains are seen on the Moon antipodal to the Imbrium and Orientale basins (e.g., Wilhelms 1987), and it is thought that intense seismic waves might have been focused on the far side during the basin-forming event, causing complex patterns of disruption (e.g., Schultz and Gault 1975; Hughes et al. 1977). Unknown is the relative role of surface and interior waves, and how different interior structure might influence the patterns and degree of development of the terrain, which differs on the Moon and Mercury. An alternative hypothesis is that the terrain formed by impact basin ejecta converging at the antipodal point (Moore et al. 1974; Wilhelms and El-Baz 1977; Stuart-Alexander 1978; Wieczorek and Zuber 2001). Furthermore, clusters of crustal magnetic anomalies have been mapped at the antipodes of some

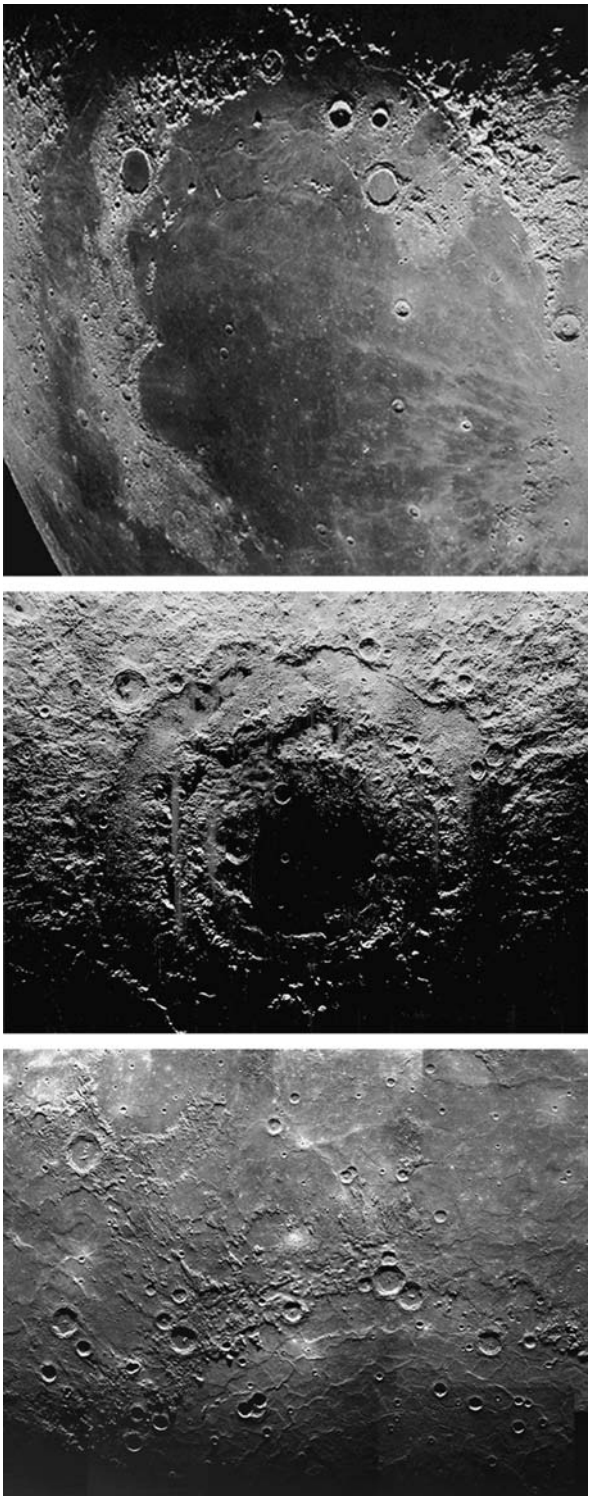

Fig. 12 The Caloris basin on Mercury, compared with the Orientale and Imbrium lunar impact basins. *Left*, the Caloris basin, 1,340 km in diameter. *Center*, the lunar Orientale basin, about 900 km in diameter and almost completely unfilled by subsequent lavas (Lunar Orbiter photograph). *Right*, in contrast to Orientale and more similar in appearance to Caloris, the Imbrium basin on the Moon, about 1,200 km diameter, is filled with several kilometers of mare lavas (Lick Observatory photograph)

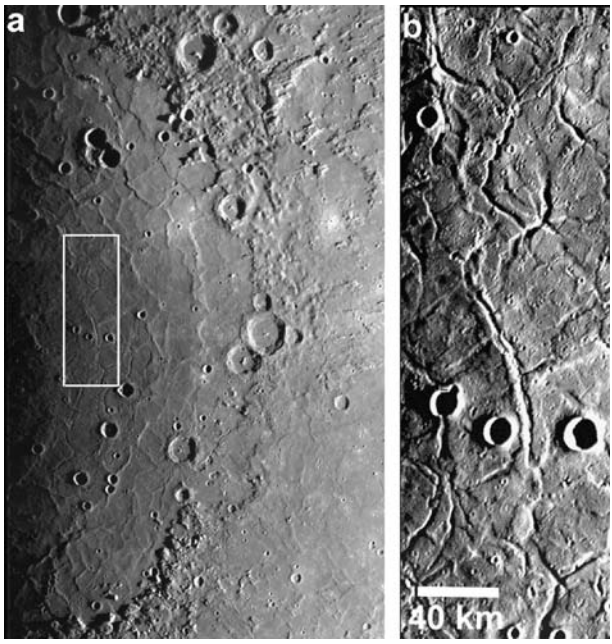

Fig. 13 The Caloris basin interior. (**a**) The interior plains of the Caloris basin have contractional (wrinkle ridges) and extensional (troughs) tectonic landforms. (**b**) High-resolution image of the interior plains showing extensional troughs that form giant polygons. Area is shown by *white box* in (**a**) (Mariner 10 image 0529055)

lunar impact basins, suggesting a relationship between crustal magnetization and antipodal basin effects (Hood 1987; Lin et al. 1988; Richmond et al. 2005). Thus, MESSENGER data on detailed unit characteristics, crustal magnetic anomalies, and the gravity and internal structure of Mercury will help to shed light on this significant but poorly known phenomenon.

The smooth plains that fill the interior of the imaged side of the Caloris basin have been heavily deformed. Basin-concentric and basin-radial wrinkle ridges are crosscut by a complex pattern of narrow extensional troughs (Fig. 13) (Strom et al. 1975; Dzurisin 1978; Melosh and McKinnon 1988; Watters et al. 2005). In plan view, the troughs are highly variable; some are linear while others are very sinuous, forming a polygonal pattern that strongly resembles giant polygons subsequently found in polygonal terrain on Mars and Venus (Carr et al. 1976; Pechmann 1980; McGill 1986; Hiesinger and Head 2000; Johnson and Sandwell 1992; Smrekar et al. 2002). The Caloris polygonal troughs are distributed in an arc ~180 km from the basin rim, extending inwards ~450 km towards the basin center (Fig. 13). How far the troughs extend into the unimaged hemisphere is currently unknown; however, the location of the most prominent polygonal troughs suggests that the peak extensional strain is ~180 to 450 km from the basin rim (Watters et al. 2005).

Giant polygons in the interior of the Caloris basin are in sharp contrast to lunar maria where trough-forming graben are found near the margins or outside the basins (McGill 1971; Strom 1972; Maxwell et al. 1975; Golombek 1979). This lunar pattern is thought to be due to loading from relatively dense, uncompensated volcanic-fill-inducing flexure of the lithosphere and resulting in interior compression and extension on the margins (Phillips et al. 1972; Melosh 1978; Solomon and Head 1979, 1980; Freed et al. 2001). Further, the crosscutting relationships between wrinkle ridges and polygonal troughs indicate that extension in Caloris postdates contraction (Strom et al. 1975; Dzurisin 1978; Melosh and McKinnon 1988). The wrinkle ridges in the interior fill material of Caloris and in the smooth plains exterior to the basin are likely to have formed in response to sub-

sidence of the interior fill material (see Melosh and McKinnon 1988), possibly aided by a compressional stress bias in the lithosphere due to global contraction (see Watters et al. 2004, 2005). Basin-interior extension, however, is not consistent with mascon tectonic models (see Freed et al. 2001). Interior extensional stresses may have resulted from exterior annular loading due to the emplacement of the expansive smooth plains adjacent to Caloris (Melosh and McKinnon 1988). This annular load could cause basin-interior extension and concentric normal faulting. Alternatively, the Caloris troughs may have formed from lateral flow of a relatively thick crust toward the basin center (Watters et al. 2005). Lateral crustal flow causes late-stage basin uplift and extension consistent with the location and magnitude of the stresses inferred from the polygonal troughs. The MESSENGER mission will obtain imaging, mineralogy, and altimetry data (Table 1) to document the temporal and spatial relationships of these units and structures in order to assess their origin and evolution. Furthermore, the new MESSENGER data will provide extensive detection of other basins and craters, and their geological and geophysical characteristics, in the unimaged portion of Mercury (e.g., Harmon et al. 2007).

5 Geological Processes on Mercury: Tectonism

The style and evolution of tectonism on a planetary body provide important information on the lateral continuity, thickness, and lateral and vertical movement of the lithosphere in space and time (Head and Solomon 1981). The geological record of tectonism on planetary surfaces contains information on the style, timing, and magnitude of deformation, the candidate causative processes and the relation to global thermal evolution. Indeed, a well-constrained global history of tectonism may permit a much more refined understanding of the formation and evolution of Mercury's core, its spin-orbit history, and the origin of its magnetic field (e.g., Zuber et al. 2007).

Tectonic features are a manifestation of the stress history of crustal and lithospheric materials on solid planetary bodies. Compressional and extensional stresses result in a variety of tectonic landforms. Crustal extension results in normal faults, graben, and rifts [e.g., graben on the Moon (McGill 1974); rift zones on Mars (Lucchitta et al. 1992) and Venus (Solomon et al. 1992; Basilevsky and Head 2002)], while compression results in folds, thrust faults, and high-angle reverse faults [e.g., wrinkle ridges and lobate scarps on Mars (Watters 1988, 1991, 1993, 2003; Golombek et al. 2001), fold belts on Venus (Basilevsky and Head 2000)]. Furthermore, compressional and extensional features are often found in and around areas of inferred mantle upwelling and downwelling [e.g., circum-corona structures on Venus (Stofan et al. 1997)], or lithospheric loading [e.g., deformation surrounding mare loads on the Moon (Solomon and Head 1980) and the Tharsis Rise on Mars (Banerdt et al. 1992)]. The combination of knowledge of the style, timing, and magnitude of deformation has permitted the distinction between histories dominated by segmented and laterally interacting lithospheres, such as the plate tectonic system on Earth, and one-plate planetary bodies (Solomon 1978), such as the Moon, Mars, and Mercury, dominated by an unsegmented continuous global lithosphere. One-plate planets are characterized by evolutionary thickening of the lithosphere and predominantly vertical deformation (upwelling, loading) (Head and Solomon 1981).

One of the major surprises of the Mariner 10 mission was the presence of widespread evidence of hemisphere-scale crustal deformation (Strom et al. 1975). Tectonic landforms are distributed throughout highland and lowland plains and the floor of the Caloris basin, in the ancient intercrater plains and in the youngest smooth plains. The dominant form of

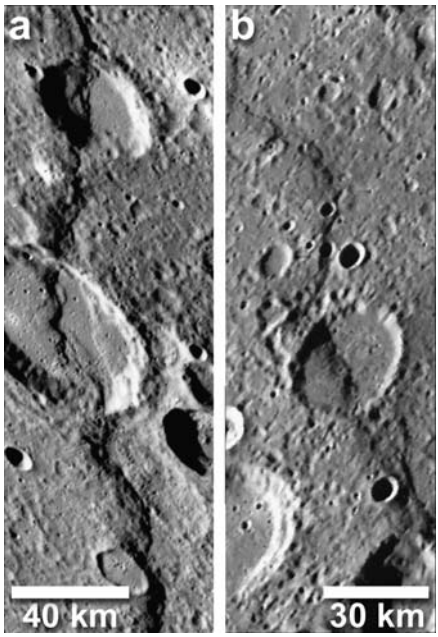

Fig. 14 Lobate scarps in the hemisphere of Mercury imaged by Mariner 10. (**a**) Discovery Rupes [~55°S, 323°E (37°W)] and (**b**) Santa Maria Rupes [~4°N, 340.5°E (19.5°W)] are two of the most prominent lobate scarps, landforms interpreted to be the surface expressions of thrust faults (Mariner 10 images 0528884 and 0027448)

deformation in the imaged hemisphere of Mercury is crustal shortening, expressed by three landforms: lobate scarps, wrinkle ridges, and high-relief ridges. Lobate scarps are linear or arcuate in plan view and asymmetric in cross-section, with a steeply sloping scarp face and a gently sloping back scarp (Strom et al. 1975; Cordell and Strom 1977; Dzurisin 1978; Melosh and McKinnon 1988; Watters et al. 1998, 2001, 2002). The asymmetric morphology and evidence of offset crater floors and walls indicate that lobate scarps are the expression of surface-breaking thrust faults (Fig. 14) (Strom et al. 1975; Cordell and Strom 1977; Melosh and McKinnon 1988; Watters et al. 1998, 2001, 2002, 2004). Topographic data derived from Mariner 10 stereo pairs indicate that the longest known lobate scarp, Discovery Rupes (~500 km), also has the greatest relief (~1.5 km) (Fig. 14) (Watters et al. 1998, 2001).

Wrinkle ridges are generally more complex morphologic landforms than lobate scarps (Fig. 15), often consisting of a broad, low-relief arch with a narrow superimposed ridge (Strom 1972; Bryan 1973; Maxwell et al. 1975; Plescia and Golombek 1986; Watters 1988). These two morphologic elements can occur independently of one another, and for wrinkle ridges in the imaged hemisphere of Mercury, this is the rule rather than the exception (see Strom et al. 1975). Although the consensus is that wrinkle ridges are the result of a combination of folding and thrust faulting, the number and the geometry of the faults involved are not obvious (see Schultz 2000; Gold et al. 2001; Watters 2004). Mercury's known wrinkle ridges are predominantly found in the floor material of the Caloris basin and in the smooth plains surrounding the basin.

High-relief ridges are the rarest of the contractional features (Watters et al. 2001). Commonly symmetric in cross-section, high-relief ridges have greater relief than wrinkle ridges (Fig. 16). Topographic data show that the high-relief ridge informally named Rabelais Dorsum (Fig. 16) has a maximum relief of ~1.3 km. Some high-relief ridges, like Rabelais Dorsum, transition into lobate scarps (Fig. 16), suggesting that they are also fault-controlled structures, possibly the surface expression of high-angle reverse faults (Watters et al. 2001).

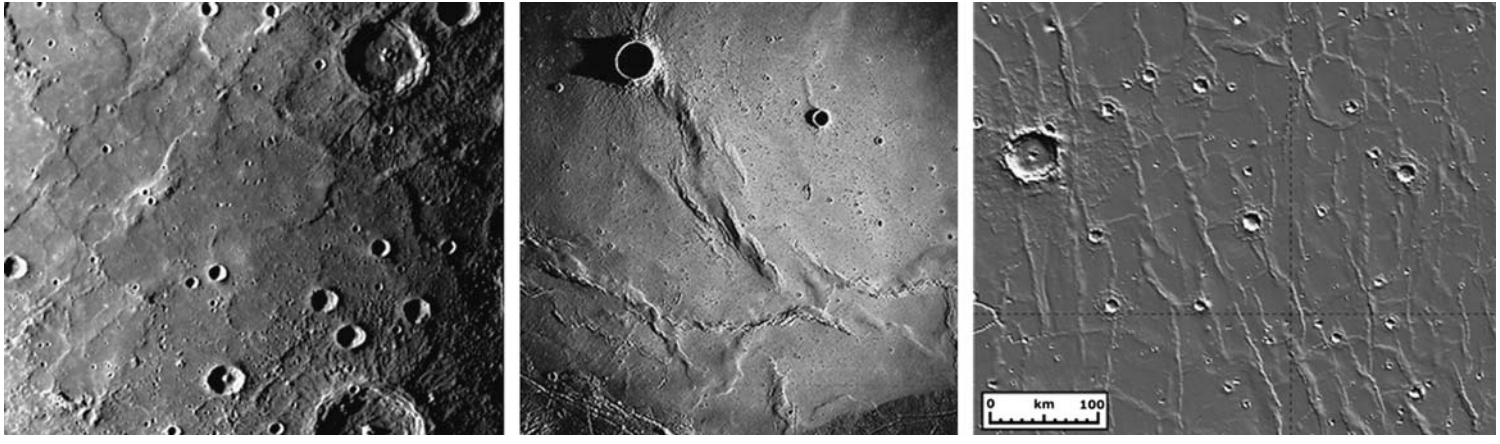

Fig. 15 Wrinkle ridges on the plains of Mercury and similar features on the Moon and Mars. *Left*, wrinkle ridges in the plains of Mercury. View is ~385 km in width (Mariner 10 image 0000167). *Middle*, the southern part of lunar Mare Serenitatis showing the development of wrinkle ridges in the mare basalts. View is ~70 km in width (Apollo image). *Right*, wrinkle ridges in Lunae Planum on the eastern part of the Tharsis rise (MOLA digital topographic image). Note the similarities in the ridges in terms of general trends, separation, convergence, cross-cutting, and circularity around apparently buried craters

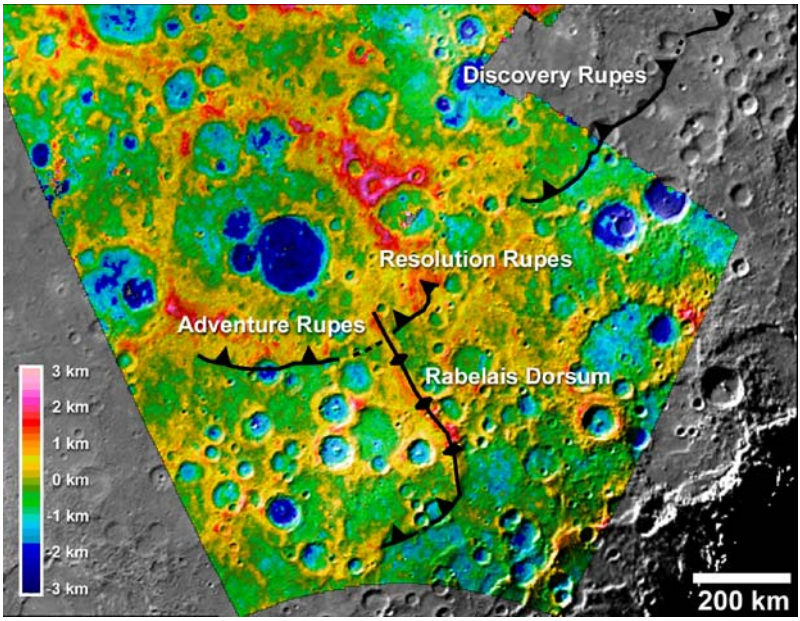

Fig. 16 Topographic expression of some prominent tectonic features in the southern hemisphere of Mercury. The digital elevation model was generated from Mariner 10 stereo pairs (see Watters et al. 2001) and is overlaid on an image mosaic. The locations of Discovery Rupes, Resolution Rupes, Adventure Rupes (all lobate scarps), and Rabelais Dorsum (a high-relief ridge) are shown. Thrust fault dip directions are indicated by *black triangles*. The mosaic covers 50°−75°S and 335°−280°E (25–80°W). Elevations are relative to a 2,439.0-km-radius sphere

One of the remarkable aspects of tectonics on Mercury is the absence of clear evidence of extension in the hemisphere imaged by Mariner 10 outside the Caloris basin. More subtle evidence of extension may occur in the form of a fabric of fractures that make up what has been described as a tectonic grid (Dzurisin 1978; Melosh and McKinnon 1988). This tectonic grid is expressed by lineaments that may reflect ancient lines of weakness in the lithosphere (Melosh and McKinnon 1988).

Of the tectonic features on Mercury, lobate scarps are the most widely distributed spatially (Fig. 17). An accurate assessment of the spatial distribution of the lobate scarps is difficult because the distribution may be strongly influenced by observational bias introduced by variations in the lighting geometry across the imaged hemisphere (see Cordell and Strom 1977; Melosh and McKinnon 1988; Thomas et al. 1988). The incidence angle of Mariner 10 images changes from 90° at the terminator to 0° at the subsolar point. Thus, only a small percentage of the imaged hemisphere has an optimum lighting geometry for the identification of lobate scarps or other tectonic features. However, recent mapping suggests that the distribution of lobate scarps is not uniform, even in areas where the incidence angle is optimum (>50°) (Watters et al. 2004). More than 50% of the area-normalized cumulative length of lobate scarps occurs south of 30°S, with the greatest cumulative length between 50°S and 90°S (Watters et al. 2004) (Fig. 17). The dip directions of the thrust faults inferred from the hanging wall-foot wall relationship suggests that there is no preferred thrust slip direction north of 50°S (Fig. 17). South of 50°S, however, the lobate scarp faults all dip to the north, NW, or NE; none dip southward (Fig. 17) (Watters et al. 2004). This indicates that

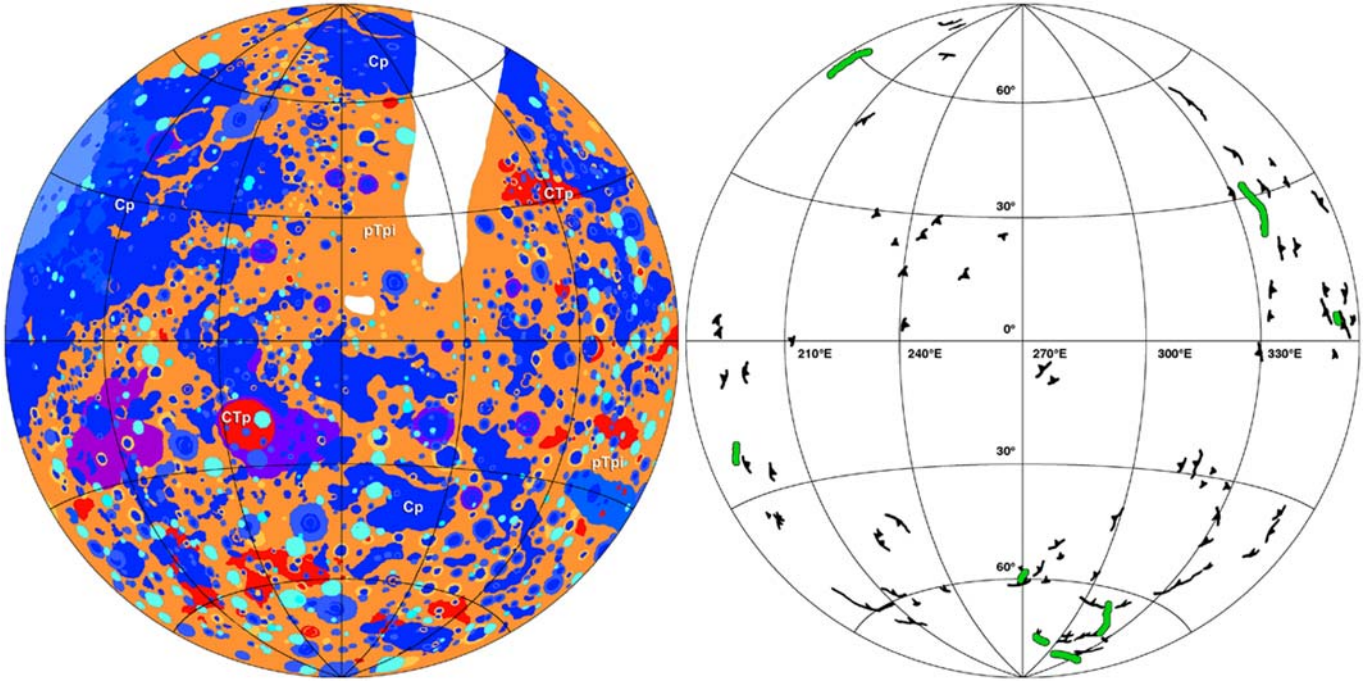

Fig. 17 Location of lobate scarps and high-relief ridges in the hemisphere of Mercury imaged by Mariner 10. The geologic map of Mercury (Spudis and Guest 1988) (*left*) provides context for the location of the lobate scarps and high-relief ridges (*right*). Major geologic units are intercrater plains material pTpi (*tan*), Calorian-Tolstojan plains material CTp (*red*), and Calorian plains material Cp (*blue*). Lobate scarps are *black* (thrust fault dip directions are indicated by *black triangles*), and high-relief ridges are in *green*

across a broad zone in the southern hemisphere, there is a preferred southward thrust dip direction.

The age of the lobate scarps is not well constrained. Lobate scarp thrust faults clearly deform the oldest plains material, pre-Tolstojan intercrater plains emplaced near the end of the period of heavy bombardment. Thus, the earliest preserved record of lobate scarp formation occurred near or after the end of heavy bombardment (Strom et al. 1975). Lobate scarps are also found in younger Tolstojan and Calorian-aged smooth plains units, suggesting that thrust faulting continued after the formation of the Caloris basin and the emplacement of the youngest smooth plains (Fig. 17) (Strom et al. 1975; Melosh and McKinnon 1988). If lobate scarps were uniformly distributed in the imaged hemisphere, their absence in hilly and lineated terrain antipodal to the Caloris basin would suggest that most of the scarps were pre-Caloris in age (Cordell and Strom 1977). Several lines of evidence, however, suggest a Calorian age of formation for the lobate scarps. First, lobate scarps are not uniformly distributed outside the hilly and lineated terrain (Fig. 17). Second, there is no evidence of embayment of scarps by ancient intercrater plains (Strom et al. 1975; Melosh and McKinnon 1988) or by younger Tolstojan and Calorian smooth plains materials (Watters et al. 2004). Third, while lobate scarp thrust faults often cut across and offset the floors and rim walls of large impact craters (Fig. 14), there are no incidences of large craters superimposed on scarps. Fourth, there is no apparent degradation or partial burial of lobate scarps by Caloris ejecta in the northern hemisphere (Watters et al. 2004). Thus, all the lobate scarps in the imaged hemisphere may have formed after the emplacement of the Calorian smooth plains (Watters et al. 2004).

Mechanisms for the formation of the lobate scarps include global contraction due to interior cooling, tidal despinning, a combination of thermal contraction and despinning, and the interaction of thermal stresses and stresses related to the Caloris basin (Strom et al. 1975; Cordell and Strom 1977; Melosh and Dzurisin 1978a, 1978b; Pechmann and Melosh 1979; Melosh and McKinnon 1988; Thomas et al. 1988). Slow thermal contraction of the planet from secular cooling of the interior is predicted to result in global, horizontally isotropic compression (Solomon 1976, 1977, 1978, 1979; Schubert et al. 1988; Phillips and Solomon 1997; Hauck et al. 2004). Thermal models predict the onset of lithospheric contraction before the end of the period of heavy bombardment (Solomon 1977; Schubert et al. 1988). Slowing of Mercury's rotation by despinning due to solar tides and the relaxation of an early equatorial bulge is predicted to induce stresses in the lithosphere (Melosh 1977; Melosh and Dzurisin 1978a; Pechmann and Melosh 1979; Melosh and McKinnon 1988). Stresses from tidal despinning predict E–W compression in the equatorial zone and N–S extension in the polar regions (Melosh 1977). The rapid spindown model suggests that despinning and thermal contraction thus may have been coincident and the stresses coupled (Pechmann and Melosh 1979; Melosh and McKinnon 1988). The formation of the Caloris basin may have influenced the pattern of tectonic features by introducing stresses that interacted with existing lithospheric stresses from thermal contraction (Thomas et al. 1988). This interaction might have temporarily reoriented stresses and resulted in the formation of Caloris-radial thrust faults.

All the models described here have limitations in explaining the spatial and temporal distribution of the lobate scarps. Although the orientation of wrinkle ridges in the smooth plains exterior to the Caloris basin may have been influenced by basin-related stresses, few lobate scarps in the imaged hemisphere are radial to Caloris (Fig. 17). Tidal despinning predicts a system of normal faults in Mercury's polar regions that have not been observed (Solomon 1978; Schubert et al. 1988; Melosh and McKinnon 1988; Watters et al. 2004). In the absence of other influences, thermal contraction would be

expected to generate a uniform distribution of thrust faults with no preferred orientation and no preferred thrust slip direction (Watters et al. 2004). The amount of crustal shortening expressed by lobate scarps is another important constraint. Strom et al. (1975) estimated a reduction in planetary radius of ∼1−2 km assuming an average displacement of 1 km for the total length of the lobate scarps mapped over an area covering ∼24% of the surface. From displacement–length (*D–L*) relationships of the thrust faults, the strain expressed by the lobate scarps in an area covering ∼19% of the surface has been estimated to be ∼0.05%, corresponding to a radius decrease of <1 km (Watters et al. 1998). This is consistent with estimates obtained using all the known lobate scarps in the imaged hemisphere (Fig. 17). Such low values of strain and radial contraction are difficult to reconcile with existing thermal contraction models and may indicate that only a fraction of the total strain due to interior cooling is expressed by the observed thrust faults, or that the earliest activity is obscured by the cratering flux or intercrater plains. Other tectonic features such as long-wavelength lithospheric folds (Dombard et al. 2001; Hauck et al. 2004) or small-scale faults that are difficult to detect with existing image data may account for the strain deficit. Similar, broad contractional belts are seen on Venus (e.g., Frank and Head 1990) but differ in morphology in that evidence for extensive thrusting and surface shortening is not as apparent.

Conspicuously absent from the portion of Mercury seen thus far are features that might be attributed to large mantle swells or voluminous mantle-derived magmatism (such as the Tharsis region of Mars) and intermediate-scale mantle activity (such as coronae on Venus). The relatively thin (∼500 km) mantle of Mercury may have limited the length-scale of mantle-driven tectonism. With the exception of the interior of the Caloris basin, also absent is evidence for extensive lithospheric loading and flexural deformation (as seen on the Moon and Mars) and large-scale features indicative of extensional deformation (such as graben and rifts seen on the Moon, Venus, and Mars). The common occurrence of crustal heterogeneities and asymmetries on Mars, the Moon, and Venus suggest that it is unwise to conclude at present that the other half of Mercury will be the same as the hemisphere seen by Mariner 10.

The MESSENGER mission (Table 1) will provide regional- to global-scale altimetry and imaging data that will permit the quantitative characterization of the tectonic features on the part of Mercury unimaged by Mariner 10 and allow a quantitative global assessment of tectonic features in order to derive more rigorous estimates of the style, timing, and magnitude of deformation, the candidate causative processes, and the relation to global thermal and interior evolution (e.g., Nimmo 2002; Nimmo and Watters 2004).

6 Geological Processes on Mercury: Volcanism and Plains Formation

Volcanism, the eruption of internally derived magma, and its surface deposits, provide one of the most important clues to the location of interior thermal anomalies in space and time and to the general thermal evolution of the planet. Volcanism is among the dominant endogenic geologic process on other terrestrial planetary bodies and can produce significant resurfacing during the evolution of the body. Volcanism is a key element in the formation and evolution of secondary crusts (those derived from partial melting of the mantle) and tertiary crusts (those derived from remelting of primary and secondary crusts) (Taylor 1989).

Little is known concerning the history of volcanism on Mercury. In contrast to the Moon, where there are distinctive composition-related albedo variations between the cratered uplands (relatively high) and the smooth volcanic mare lowlands (relatively low), the albedo

of Mercury is relatively uniform across the surface. Prior to the Apollo 16 mission to the Moon in 1972, a widely distributed smooth plains unit (the Cayley Formation) was mapped in the lunar uplands, lying stratigraphically between the younger, low-albedo maria, and the older, high-albedo impact basins and cratered terrain (Wilhelms and McCauley 1971). One of the purposes of the Apollo 16 mission (Hinners 1972) was to determine the petrology and absolute age of this unit, thought prior to the mission to represent a distinctive pre-mare, highland phase of volcanism (e.g., Trask and McCauley 1972). During Apollo 16 surface operations it became rapidly clear that the Cayley Formation consisted of impact breccias (Young et al. 1972), and later assessments suggested that the deposits were a combination of local (e.g., Head 1974) and regional, basin-related impact ejecta (Oberbeck et al. 1974, 1977). On the basis of the Apollo 16 results, lunar light plains were subsequently considered by most workers to have been emplaced by impact crater and basin ejecta processes (Oberbeck 1975), rather than by extrusive volcanism (Trask and McCauley 1972). The subsequent documentation of mare volcanic deposits buried by layers of highland crater ejecta (cryptomaria; Head and Wilson 1992; Antonenko et al. 1995) as well as some local moderate-albedo units thought to be of extrusive volcanic origin (e.g., the Apennine Bench Formation; Spudis and Hawke 1986) suggested that the interpretations of light plains might be more complex than simple ejecta emplacement.

Arriving at Mercury shortly after Apollo 16, Mariner 10 revealed the presence of two smooth Cayley-plains-like units alternately interpreted to represent effusive volcanic deposits or basin ejecta. These widespread plains deposits, occurring as relatively smooth surfaces between craters (intercrater plains), and as apparently ponded material (smooth plains; Fig. 3), were proposed by some to be volcanic in origin (Murray 1975; Murray et al. 1975; Trask and Guest 1975; Strom et al. 1975; Strom 1977; Dzurisin 1978). Others argued that the plains deposits might represent basin ejecta, similar to those found at the lunar Apollo 16 landing site (Wilhelms 1976a; Oberbeck et al. 1977). Part of the problem concerning interpretation of smooth plains on Mercury as volcanic or impact in origin is the relatively low resolution of the Mariner 10 data. Early on it was pointed out that the Mariner 10 image data do not have the resolution required to resolve lunar-like volcanic features such as flow fronts, vents, and small domes (Schultz 1977; Malin 1978), a problem further explored by Milkovich et al. (2002) (Fig. 18). Detailed examination of lunar images at resolutions and viewing geometries comparable to those of Mariner 10 readily showed that small shields and cones, elongate craters, sinuous rilles and flow fronts, all hallmarks of the identification of volcanism on the Moon (e.g., Head 1976; Head and Gifford 1980), would not be resolvable in most of the Mariner 10 images (Milkovich et al. 2002). Furthermore, larger features typical of volcanism on Mars [such as huge volcanic edifices and calderas (Carr 1973; Crumpler et al. 1996)], and not seen on the Moon (Head and Wilson 1991), were not observed by Mariner 10 on Mercury. Also not observed in the Mariner 10 data were examples of the large (10–30 km diameter) steep-sided domes suggestive of crustal magmatic differentiation processes seen on the Moon (Head and McCord 1978; Chevrel et al. 1999) and Venus (Pavri et al. 1992; Ivanov and Head 1999). Lobate fronts exposed at the edge of smooth plains occurrences on Mercury (Fig. 19; arrows) suggested that these might have been volcanic flow margins, but comparisons to marginal basin ejecta deposits on the Moon indicated that such features could also be a product of impact ejecta emplacement (e.g., Milkovich et al. 2002). Thus, although the surface features observed by Mariner 10 were most similar to lunar plains, there were also fundamental differences between volcanism occurring on the two bodies (Head et al. 2000).

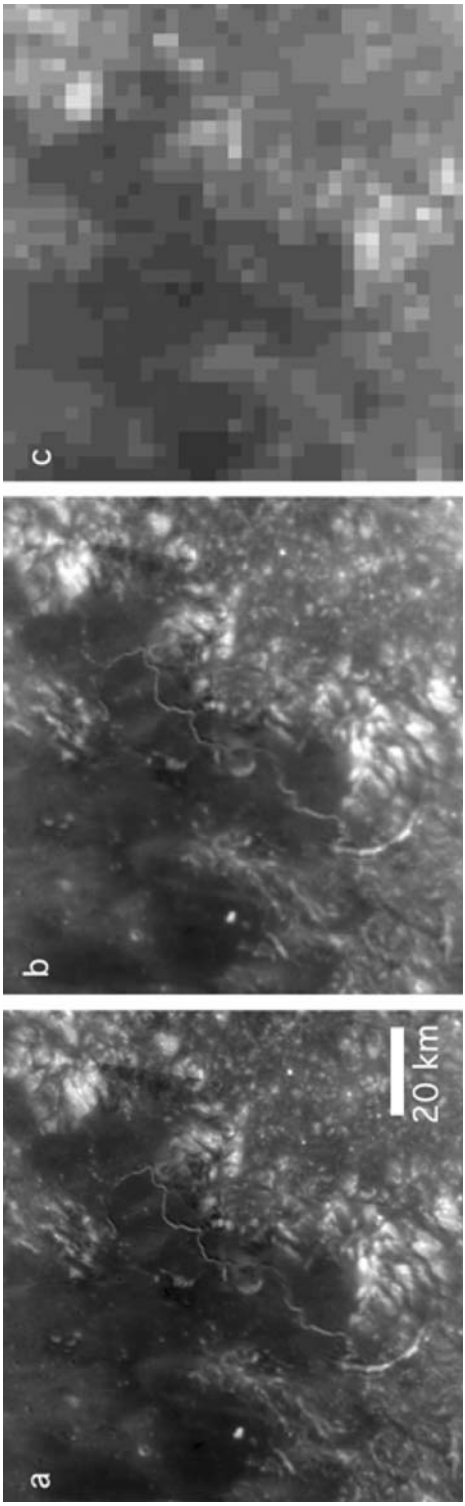

Fig. 18 Lunar volcanic features shown as a function of resolution. Hadley Rille (~25°N, 3°E) at multiple resolutions: (**a**) 100 m/pixel; (**b**) 500 m/pixel; (**c**) 2.5 km/pixel. After Milkovich et al. (2002)

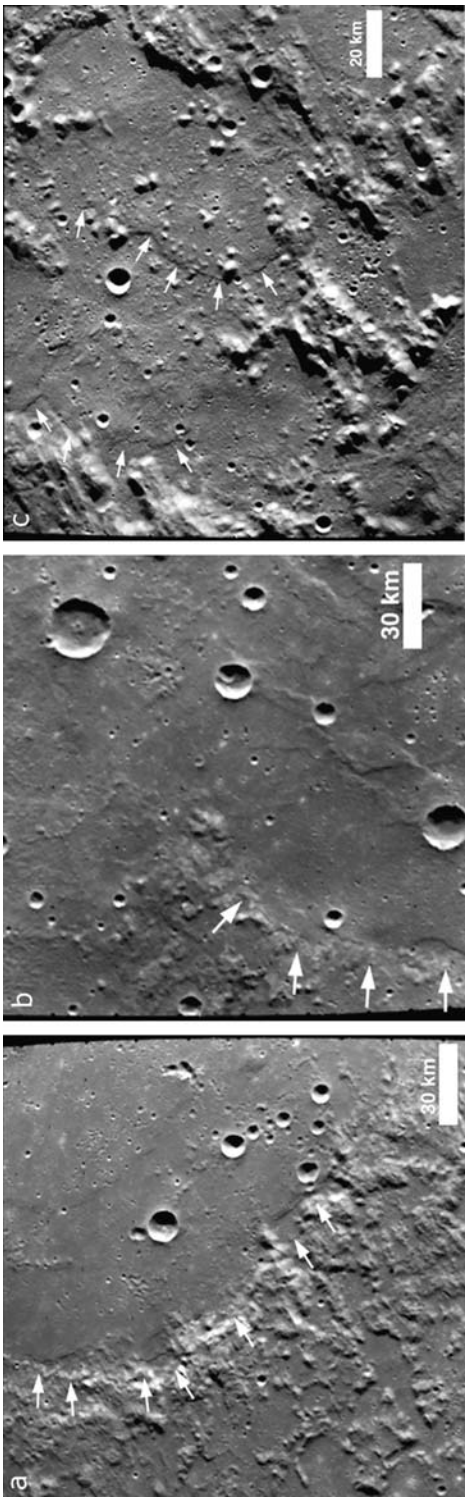

Fig. 19 Smooth plains deposits on Mercury. (**a**) Smooth plains (*middle* and *upper right* of image) embaying the inner rim of the crater Van Eyck; arrows indicate flow-like scarps. Mariner 10 image 0000077; 180 m/pixel. (**b**) Smooth plains (*lower middle* and *right* of image) in the Odin Formation. *Arrows* indicate the margin of plains that appear to embay the Odin Formation. Mariner 10 image 0000104; 280 m/pixel. (**c**) Lobate scarps in the Nervo Formation. The *arrows* indicate two lobate scarps that appear to have been emplaced by flow. Mariner 10 image 0000108; 300 m/pixel

These various observations raised the interesting possibility that there may be no identifiable volcanic units on Mercury. Crater counts of Caloris basin ejecta facies and smooth plains deposits, however, indicated that the smooth plains were emplaced after the Caloris basin (Spudis and Guest 1988) (Figs. 9 and 10), and on this basis they were interpreted to be the product of volcanic eruptions, not contemporaneous ejecta emplacement. On the other hand, the lunar Cayley plains also often showed younger ages than the adjacent textured ejecta deposits from major basins [for smaller crater diameters; see Wilhelms (1987)]. The counts of Spudis and Guest (1998) were carried out using carefully defined contiguous map units and only larger craters unaffected by secondaries. Reprocessed Mariner 10 color data (e.g., Robinson and Lucey 1997) (Figs. 4–7), as discussed earlier, provided additional evidence for the possible volcanic origin of the smooth plains.

Could extrusive volcanism not have occurred on Mercury, and if such advective cooling processes did not occur, how did the planet dissipate its accretional heat and that from subsequent decay of radioactive nuclides? Perhaps Mercury experienced styles of volcanism unknown on the Earth and Moon, and current data do not allow us to recognize such unusual deposits. Another possibility is that partial melting of the mantle may have occurred, but that extrusive volcanism did not. Investigating these possibilities, Head and Wilson (2001) assessed the ascent and eruption of magma under Mercury conditions for a range of scenarios and found that a thick low-density crust could, as with the Moon (e.g., Head and Wilson 1992), inhibit and potentially preclude dikes from rising to the surface and forming effusive eruptions. This, combined with an apparent global compressional net state of stress in the lithosphere (e.g., Strom et al. 1975), could produce a scenario in which rising magma intruded the crust but did not reach the surface to produce the level of resurfacing or the array of landforms seen on the Moon, Mars, and Venus. Indeed, Head and Wilson (2001) showed how easy it was, given the range of conditions known to occur in the history of terrestrial planetary bodies, to create a planet with little to no extrusive volcanic activity.

The fact that such fundamental questions remain concerning Mercury's thermal evolution underscores the importance of the MESSENGER mission to elucidating the early evolution of the terrestrial planets. The dominant endogenic geologic process on the Earth, Moon, Mars, and Venus is volcanism, characterized by massive extrusions of basaltic lavas, significant resurfacing of their surfaces, and emplacement of large volumes of intrusive magmas (e.g., Basaltic Volcanism Study Project 1981).

From these and related observations described earlier, it is possible to make some general inferences concerning the source regions of volcanic extrusions—the upper mantle. From terrestrial analyses it is known that FeO abundance of mantle source regions corresponds, to a first order, to the FeO content of the erupted magma (e.g., Longhi et al. 1992). The observation that candidate volcanic deposits identified on Mercury do not have FeO abundances differing from the hemispheric average indicates that the mantle source of such material is not enriched in FeO relative to the crust, or conversely that the ancient crust is not depleted in FeO relative to the upper mantle (Robinson et al. 1997, 1998). If the plains deposits had a significant increase (or decrease) in FeO relative to the basement rock that they overlie (ancient crust), then they would appear as a mappable unit in the iron-plus-maturity image and albedo (Figs. 4, 5, 6 and 7). In contrast, mare deposits found on the Moon (mare lavas versus anorthositic crust) have a significant contrast in FeO content relative to the ancient anorthositic crust they overlie [typically >15 wt% versus <6 wt%, respectively; see Lucey et al. (1998)]. The global crustal abundance of FeO on Mercury has been estimated to be less than 6 wt% from remote sensing data (McCord and Adams 1972; Vilas and McCord 1976; Vilas et al. 1984; Vilas 1985, 1988; Veverka et al. 1988; Sprague et al. 1994; Blewett et al. 1997). The lack of structures corresponding to the candidate volcanic plains units in the iron-plus-maturity image is consistent with mantle magma

source regions approximately sharing the crustal FeO composition, and so supports the idea that Mercury is highly reduced and most of its iron is sequestered in a metallic core.

Thus, if there are no significant variations in iron abundance in the areas seen by Mariner 10 one must address the question "What could be the composition of candidate volcanics on Mercury?" Komatiitic volcanics are found on the Earth with FeO abundances of under 5 wt%, as are relatively low-iron mafic lavas on the Moon in the Apennine Bench Formation (Spudis and Hawke 1986). The most likely candidate is a high-magnesium, low-iron magma. The MESSENGER mission (Table 1) will therefore not only provide very important information on the possible volcanic origin of surface plains deposits from imaging and altimetry, but it will also permit assessment of mantle characteristics and mineralogy and core evolution processes from surface mineralogy and chemistry. Superficially, Mercury looks like the Moon, but Mariner 10 and terrestrial remote sensing data tell us that it must be very different in many fundamental respects. Could Mercury be an Earth's Moon that did not undergo surface evolution by endogenic processes (e.g., mare volcanism) subsequent to the period of large basin formation?

7 Geological Processes on Mercury: Polar Deposits

One of the most impressive discoveries from Earth-based observations is the detection of high radar backscatter, strongly depolarizing deposits in the near-polar regions of Mercury (e.g., Harmon and Slade 1992; Butler et al. 1993; Harmon et al. 1994; Harmon 1997). The obliquity of Mercury is near 0° so there are extensive areas of permanently shadowed regions within fresh craters that can act as cold traps for volatile compounds. On the basis of orbital geometries, from Earth we are able to view these areas on Mercury slightly better than the polar regions on the Moon. Earth-based radar observations (Harmon et al. 2001) detected highly radar reflective deposits in these areas at both the north and south poles. The deposits occur in fresh craters as low as 72°N latitude (Fig. 20). Degraded craters do not show the high radar backscatter deposits because their interiors are exposed to the Sun. The neutron spectrometer on the Lunar Prospector spacecraft discovered enhanced hydrogen signals in permanently shadowed craters in the polar regions of the Moon (Feldman et al. 1998). This has been interpreted as water ice with a concentration of $1.5 \pm 0.8\%$ weight fraction.

The radar depolarized, highly backscattered signal is essentially identical to the intensity and characteristics of the radar backscatter signals from the martian south polar water ice cap and the icy Galilean satellites (Harmon et al. 2001). This has been used as evidence that the deposits are water ice. The permanently shadowed cold traps are essentially full, and the strong radar signals indicate that if the material is water ice then it is quite pure. The estimated thickness of the deposits is believed to be at least 2 m, but radar observations cannot set an upper limit on the thickness. The area covered by the polar deposits (both north and south) is estimated to be $\sim(3 \pm 1) \times 10^{14}$ cm^2. This is equivalent to 4×10^{16} to 8×10^{17} g of ice, or 40–800 km^3 for a deposit 2–20 m thick (Vasavada et al. 1999).

Other material has been suggested for the polar deposits including sulfur, which has radar backscatter characteristics similar to water ice, but a higher stability limit (Sprague et al. 1995). A 1-m-thick layer of water ice is stable for 10^9 years at a temperature of -161°C, while sulfur is stable at a considerably higher temperature of -55°C. Much of the region surrounding permanently shadowed craters is less than -55°C, but there are no radar reflective deposits there (Vasavada et al. 1999). Very cold silicates have also been suggested as a possibility, with the high radar response of the polar regions attributed to the decrease of dielectric loss of silicate materials with lower temperature (Starukhina 2001).

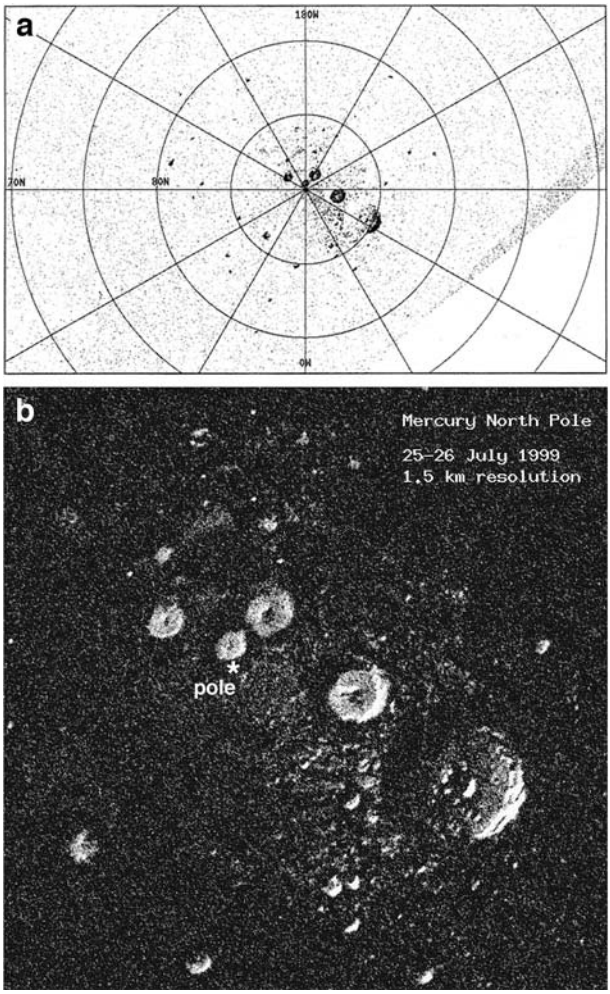

Fig. 20 Bright radar signals from localized regions in permanently shadowed craters at high northern latitudes on Mercury's surface. (**a**) Ten-microsecond north polar SC image from Arecibo radar observations on July 25–26, 1999, with a superimposed location grid. Radar illumination is from the upper left, and the region beyond the radar horizon is at lower right. (**b**) Details of the central portion of the radar image from July 25–26, 1999, in the vicinity of the north pole (see star). Resolution is 1.5 km. From Harmon et al. (2001)

If the deposits are water ice, the most likely sources of the water are micrometeoroid, comet, and water-rich asteroid impacts. If the current terrestrial influx of interplanetary dust particles is extrapolated to Mercury, over the last 3.5 billion years it could have delivered (3–60) $\times$ 10^{16} g of water ice to the permanently shadowed polar regions (an average thickness of 0.8–20 m). Impacts from Jupiter-family comets over the last 3.5 billion years could supply 0.1–200 $\times$ 10^{16} g of water to Mercury's polar regions (corresponding to an ice layer 0.05–60 m thick). Halley-type comets can supply 0.2–20 $\times$ 10^{16} g of water to the poles (0.1–8 m ice thickness). These sources alone provide more than enough water to account for the estimated volume of ice at the poles (Moses et al. 1999). The ice deposits could, at least in part, be relatively recent deposits, if the two radar features A and B were the result of recent comet or water-rich asteroid impacts. Crider and Killen (2005) estimated that if the polar ice deposits are both clean and buried by ~20 cm of regolith, then they must have been emplaced less than ~50 My ago.

Barlow et al. (1999) tested for the presence of subsurface ice by comparing the differences in depth/diameter relationships between high-latitude and low-latitude craters and

found no evidence for variations or the presence of "terrain softening" ground ice. Vilas et al. (2005), using shadow measurements, examined the depth-diameter relationships of 12 near-north polar craters containing polar deposits; they found that these craters are shallower by about one third than craters of comparable diameter in the general population. For a single 30-km-diameter crater, the shallowing amounts to ~900 m, representing more than 600 km^3 of material. This volume of infilling material is significantly greater than that predicted by proposed mechanisms for the emplacement by either sulfur or water ice. If these measurements are correct, then these craters, dating from the Mansurian Period (perhaps ~3–3.5 Ga), have been preferentially shallowed and have accumulated radar-anomalous material on the permanently shadowed parts of their floors. A satisfactory mechanism for such a process is unknown. The MESSENGER mission will use laser altimetry, neutron spectrometry, high-resolution imaging, and elemental and mineralogical remote sensing to verify these measurements and assess processes of crater floor fill.

8 The Geological History of Mercury: Impact Cratering Rates and the Absolute Time Scale

The heavily cratered surfaces of the Moon, Mars, and Mercury all have similar crater size/frequency distributions that probably represent the period of late heavy bombardment (LHB) early in Solar System history (Fig. 21). The population of impactors during the LHB is widely thought to have been similar throughout the inner Solar System (to within differences in encounter probabilities and energies), and the same is thought to be true for the later and different population of impactors subsequent to the LHB. The LHB period ended at ~3.8 Ga on the Moon and may have ended about the same time on Mercury. A notable difference between the lunar curve and those for Mercury and Mars is that at diameters less than about 50 km there is a paucity of craters on Mercury and Mars compared with the

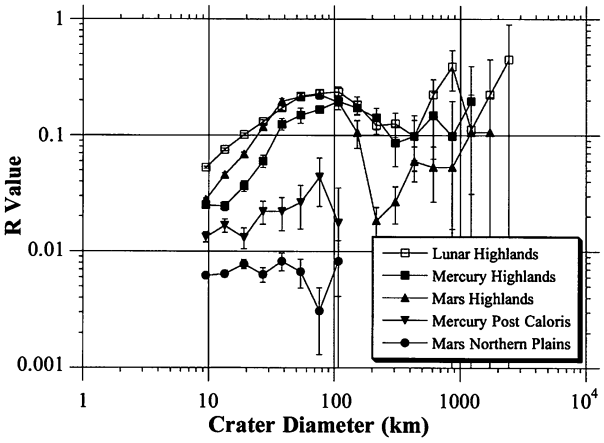

Fig. 21 Comparative impact crater size-frequency distributions. This "*R* plot," obtained by removing an inverse cubed power-law from the observed frequency versus diameter, is a comparison of the crater size/frequency distribution of the heavily cratered highlands on the Moon, Mercury, and Mars. All three have a similar shape, perhaps indicating a common origin. The steeper slopes for Mercury and Mars at smaller diameters reflect loss processes discussed in the text. Also shown is the size distribution of the post-Caloris crater population. The *bottom curve* represents the comparatively less cratered, relatively younger surfaces on Mars that have a distinctly different crater size/frequency distribution. After Strom et al. (2005)

Moon. This is usually interpreted, for Mars, as reflecting the loss of smaller craters due to erosion and infilling processes early in the post-LHB history of Mars. In the case of Mercury, it has been suggested that formation of thin but extensive so-called intercrater plains may be responsible for the loss of smaller craters. It is not yet clear why such plains should be so pervasive on Mercury, yet quite rare on the Moon. Intercrater plains are the most common terrain type on at least the part of Mercury viewed by Mariner 10 (Fig. 9). On Mercury only about 25% of the surface was viewed by Mariner 10 at Sun angles low enough to perform reliable crater counts. Unfortunately, Mariner 10 resolution is only about 1 km/pixel, so large counting areas are needed to obtain reliable statistics. These areas include the Mercury highlands and the plains within and surrounding the Caloris basin.

The smooth plains surfaces that surround and fill the Caloris basin may also show a crater size/frequency distribution similar to that of the lunar highlands, but at a lower density (Fig. 21). This post-Caloris curve may be less steep in part because it has not been affected by plains emplacement as has the highlands. Strom et al. (2005) interpreted the lower crater density to indicate that the post-Caloris surface is younger than the highlands and suggest that it formed near the end of the late heavy bombardment.

Surfaces younger than the LHB have a different crater size/frequency distribution on the Moon and Mars (Strom et al. 1992). The distribution is characterized by a single-slope -3 differential power-law distribution (Fig. 21). No region on Mercury imaged by Mariner 10 clearly shows the younger population, although error bars on the post-Caloris counts are nearly compatible with it and would certainly be compatible with a mixture of end-LHB craters and still more recent cratering such as that observed on the lunar maria. This could mean (e.g., Strom et al. 2005) that the surfaces available for crater counts in Mariner 10 images are all older than about 3.8 Ga. Perhaps there are more pristine, younger surfaces on the 55% of the planet that will be available for study from future MESSENGER images.

One can measure the relative ages of geological units on planetary surfaces from the spatial densities of superposed impact craters. "R values" represent a type of spatial density measurement (e.g., Strom et al. 2005). For example, an R value of 1 basically means that 100% of an area is covered by craters of that general diameter; an R value of 0.01 means that craters cover about 1% of the area. R values of craters on Mercury 40–100 km in diameter (Fig. 21) are roughly five times lower for post-Caloris surfaces than for the highlands. If one knows the rate at which craters are formed, and how that rate has changed with time, then the absolute age of a surface can be determined. The rate of crater formation depends on the relative proportions of different classes of impactor (e.g., comet or asteroid) that have impacted the planet. Estimates of these factors contain large uncertainties and, therefore, the estimated absolute ages are very uncertain. If the LHB was a cataclysmic event lasting only 50 or 100 My around 3.9 Ga that saturated the surfaces of the terrestrial planets, then the cratering record prior to that event has been lost (Tera et al. 1974; Ryder 1990; Kring and Cohen 2002).

More recently, the terrestrial planets have been impacted by a population of collisional fragments derived from the main asteroid belt by a variety of dynamical processes (including resonances and the Yarkovsky effect), plus some contribution of smaller comets, that presumably have impacted not only the Moon but all the terrestrial planets, although conceivably in somewhat different proportions. Another possibility for Mercury (Leake et al. 1987) is that a population of so-called vulcanoids, orbiting the Sun in the vicinity of Mercury's orbit, has preferentially cratered Mercury, but with little influence on the other terrestrial bodies. Searches for vulcanoids have not yet been successful. A vulcanoid population may be modest today, or even totally depleted, but vulcanoids could have cratered Mercury during post-LHB times, shifting much of Mercury's inferred chronology from epochs around

the LHB to more recent times. Indeed, Vokrouhlicky et al. (2000) calculated that the depletion of a vulcanoid population mediated by the Yarkovsky effect might occur on the time scale of about a billion years. On the other hand, vulcanoids may never have existed at all. If vulcanoids never existed and the LHB was an inner-solar-system-wide phenomenon, then the crater age of Mercury's highlands is about 3.9 Ga (the absolute ages of the rocks may be older), while the more lightly cratered Caloris plains are probably closer to about 3.8 Ga, to the degree that they still show the signature of the LHB.

Another source of uncertainty concerning the origin and ages of Mercury's craters is the role of large secondary craters from Mercury's numerous basins. It is possible that many or most of Mercury's craters up to 25 km in size or larger are secondaries formed by massive ejecta from the dozens of large impact basins on Mercury, as has been advocated for the Moon by Wilhelms (1976b). Although this perspective is not widely accepted, it has not been disproven and should also be assessed in MESSENGER imaging.

Thus MESSENGER is absolutely crucial to determining the impactor flux in the inner solar system and both absolute and relative ages, and therefore the chronology of the geological evolution of the surface of Mercury. Some geological features (e.g., the lobate scarps) are believed to reflect the geophysical evolution of the planet (e.g., global contraction during cooling of the interior), while the wide range of plains deposits may hold the key to whether volcanism has played a significant role in the evolution of Mercury, and if so, on what time scales. It is vital that MESSENGER data be used to study the wide range of cratering-related issues that were raised and certainly not firmly settled by Mariner 10 and subsequent Earth-based studies of Mercury.

9 Geological Processes and Evolution and Outstanding Questions

This review of our current knowledge of the nature of the surface of Mercury, the geological processes operating there, and the geological history implied by their sequence of events and relative importance with time sets the stage for a series of outstanding questions that can be addressed by the MESSENGER mission and its suite of instruments (Table 1). Among these critical questions are: What is the distribution of geological features and units in the 55% of the planet not imaged by Mariner 10? Will new discoveries made in this current terra incognita change our view of the dominant processes on Mercury and the resulting geological history? Will the considerably higher-resolution MESSENGER images reveal the presence of extensive volcanic source regions that could confirm a magmatic source for the smooth plains of Mercury? Will there be distinctive mineralogical differences between different occurrences of smooth plains or between smooth plains and intercrater plains? Will studies of crater populations sort out contributions due to asteroids, comets, possible vulcanoids, and secondary craters? Will crater counts in the unimaged terrain show evidence for the presence of post-$\sim$3.7-Ga planetary resurfacing? Will multispectral images and spectrometer data of various deposits and landforms show evidence that can be interpreted in terms of crustal thickness, structure, and vertical and lateral heterogeneity? Will tectonic features discovered on the other half of the planet support the current view of a global net compressional state of stress in the lithosphere over most of geological time? Will any evidence for extensional deformation unrelated to basin deformation be found? Could the unimaged portion of Mercury be characterized solely by extensional features, balancing the contractional features on the imaged portion? Has the sign and magnitude of global stress changed with time? What clues to the nature and thickness of the lithosphere, and how it has changed with time, can be deduced from altimetric, gravity, and imaging data on crater, basin, and

tectonic landforms? Will the presence of ice be confirmed in permanently shadowed zones in crater interiors of the polar regions? Will the unusual depth relationships of impact craters with near-polar radar anomalies determined from Mariner 10 shadow measurements be confirmed by MESSENGER altimetry? Will these same craters show any unusual mineralogical characteristics relative to those without radar anomalies? Can MESSENGER impact crater studies reveal details of impact melt generation and its fate in this high-velocity impact environment? Can the full complement of MESSENGER data extend morphologic and morphometric studies sufficiently to establish differences in substrate characteristics and to help further in distinguishing the relative roles of impact velocity, gravity, and substrate characteristics in the impact cratering process? Do any detected crustal magnetic anomalies relate to geologic features and structures? Can evidence distinguishing crustal and dynamo origins for the magnetic field be obtained (e.g., Stanley et al. 2005), and if so, what are the implications for crustal formation processes and the history of mantle convection? The complement of instruments on the MESSENGER spacecraft (Table 1), described elsewhere in this volume, will provide the data necessary to address and, in many cases answer, these fundamental questions. The MESSENGER mission, together with BepiColombo (Grard et al. 2000) and future missions (e.g., Schulze-Makuch et al. 2005), will bring new insights into key processes in planetary formation and evolution.

Acknowledgements We gratefully acknowledge the team of NASA and MESSENGER managers, engineers, and scientists who have worked together to make this mission a reality. The MESSENGER mission is supported by NASA's Discovery Program through a contract with the Carnegie Institution of Washington. This work has been supported in part by Carnegie Institution of Washington Contract DTM-3250-05. We also thank James Dickson, Anne Côté, and Peter Neivert for help in manuscript preparation. We thank Sean Solomon, Paul Spudis, Dave Blewett, Jeff Gillis-Davis, and an anonymous reviewer for excellent reviews that helped to improve the paper.

References

B.J. Anderson et al., Space Sci. Rev. (2007, this issue). doi:10.1007/s11214-007-9246-7
J.D. Anderson, R.F. Jurgens, E.L. Lau, M.A. Slade III, G. Schubert, Icarus **124**, 690–697 (1996)
G.B. Andrews et al., Space Sci. Rev. (2007, this issue). doi:10.1007/s11214-007-9272-5
I. Antonenko, J.W. Head, J.F. Mustard, B.R. Hawke, Earth, Moon Planets **69**, 141–172 (1995)
W.B. Banerdt, M.P. Golombek, K.L. Tanaka, in *Mars*, ed. by H.H. Kiefer, B.M. Jakosky, C.W. Snyder, M.S. Matthews (University of Arizona Press, Tucson, 1992), pp. 249–297
N.G. Barlow, R.A. Allen, F. Vilas, Icarus **141**, 194–204 (1999)
Basaltic Volcanism Study Project, *Basaltic Volcanism on the Terrestrial Planets* (Pergamon, New York, 1981), 1286 pp
A.T. Basilevsky, J.W. Head, J. Geophys. Res. **105**, 24583–24611 (2000)
A.T. Basilevsky, J.W. Head, J. Geophys. Res. **107**, 5041 (2002). doi:10.1029/2000JE001471
S.K. Bhattacharya, J.N. Goswami, D. Lal, P.P. Patel, M.N. Rao, *Proc. Lunar Science Conf. 6th*, 1975, pp. 3509–3526
D.T. Blewett, P.G. Lucey, B.R. Hawke, G.G. Ling, M.S. Robinson, Icarus **129**, 217–231 (1997)
D.T. Blewett, B.R. Hawke, P.G. Lucey, Meteorit. Planet. Sci **37**, 1245–1254 (2002)
E. Bowell, B. Hapke, D. Domingue, K. Lumme, J. Peltoniemi, A.W. Harris, in *Asteroids II*, ed. by R.P. Binzel, T. Gehrels, M.S. Matthews (University of Arizona Press, Tucson, 1989), pp. 524–556
W.V. Boynton et al., Space Sci. Rev. (2007, this issue). doi:10.1007/s11214-007-9258-3
W.B. Bryan, *Proc. Lunar Science Conf. 4th*, 1973, pp. 93–106
B.J. Butler, D.O. Muhleman, M.A. Slade, J. Geophys. Res. **98**, 15003–15023 (1993)
M.H. Carr, J. Geophys. Res. **78**, 4049–4062 (1973)
M.H. Carr et al., Science **193**, 766–776 (1976)
J.F. Cavanaugh et al., Space Sci. Rev. (2007, this issue). doi:10.1007/s11214-007-9273-4
S.D. Chevrel, P.C. Pinet, J.W. Head, J. Geophys. Res. **104**, 16515–16529 (1999)
M.J. Cintala, J. Geophys. Res. **97**, 947–973 (1992)

P.E. Clark, R.F. Jurgens, M.A. Leake, in *Mercury*, ed. by F. Vilas, C.R. Chapman, M.S. Matthews (University of Arizona Press, Tucson, 1988), pp. 77–100
B.M. Cordell, R.G. Strom, Phys. Earth Planet. Interiors **15**, 146–155 (1977)
D. Crider, R.M. Killen, Geophys. Res. Lett. **32**, L12201 (2005). doi:10.1029/2005GL022689
L.S. Crumpler, J.W. Head, J.C. Aubele, in *Volcano Instability on the Earth and Other Planets*, ed. by W.J. McGuire, A.P. Jones, J. Neuberg. Spec. Pub. 110 (Geological Society, London, 1996), pp. 307–348
A. Danjon, Bull. Astron. J. **14**, 315–345 (1949)
R.A. De Hon, D.H. Scott, J.R. Underwood, U.S. Geol. Surv. Misc. Inv. Ser., Map I-1233 (1981)
G. de Vaucouleurs, Icarus **3**, 187–235 (1964)
A. Dollfus, M. Auriere, Icarus **23**, 465–482 (1974)
A.J. Dombard, S.A. Hauck, II, S.C. Solomon, R.J. Phillips, Lunar Planet. Sci. **32** (2001), abstract 2035
D.L. Domingue, A.L. Sprague, D.M. Hunten, Icarus **128**, 75–82 (1997)
D. Dzurisin, J. Geophys. Res. **83**, 4883–4906 (1978)
W.C. Feldman, S. Maurice, A.B. Binder, B.L. Barraclough, R.C. Elphic, D.J. Lawrence, Science **281**, 1496–1500 (1998)
S.L. Frank, J.W. Head, Earth, Moon Planets **50/51**, 421–470 (1990)
A.M. Freed, H.J. Melosh, S.C. Solomon, J. Geophys. Res. **106**, 20603–20620 (2001)
H. Frey, S.E.H. Sakimoto, J.H. Roark, Geophys. Res. Lett. **26**, 1657–1660 (1999)
D.E. Gault, J.E. Guest, J.B. Murray, D. Dzurisin, M.C. Malin, J. Geophys. Res. **80**, 2444–2460 (1975)
R.E. Gold et al., Planet. Space Sci. **49**, 1467–1479 (2001)
J.O. Goldsten et al., Space Sci. Rev. (2007, this issue). doi:10.1007/s11214-007-9262-7
M.P. Golombek, J. Geophys. Res. **84**, 4657–4666 (1979)
M.P. Golombek, F.S. Anderson, M.T. Zuber, J. Geophys. Res. **106**, 23811–23822 (2001)
R. Grard, M. Novara, G. Scoon, ESA Bull. **103**, 11–19 (2000)
M.J. Grolier, J.M. Boyce, U.S. Geol. Surv. Misc. Inv. Ser., Map I-1660 (1984)
J.E. Guest, R. Greeley, U.S. Geol. Surv. Misc. Inv. Ser., Map I-1408 (1983)
B. Hapke, J. Geophys. Res. **86**, 3039–3054 (1981)
B. Hapke, Icarus **59**, 41–59 (1984)
B. Hapke, Icarus **67**, 264–280 (1986)
B. Hapke, *Theory of Reflectance and Emittance Spectroscopy* (Cambridge University Press, Cambridge, 1993), 469 pp
B. Hapke, Icarus **157**, 523–534 (2002)
B. Hapke, C. Christman, B. Rava, J. Mosher, *Proc. Lunar Planet. Science Conf. 11th*, 1980, pp. 817–821
J.K. Harmon, Adv. Space Res. **19**, 1487–1496 (1997)
J.K. Harmon, D.B. Campbell, in *Mercury*, ed. by F. Vilas, C.R. Chapman, M.S. Matthews (University of Arizona Press, Tucson, 1988), pp. 101–117
J.K. Harmon, M.A. Slade, Science **258**, 640–642 (1992)
J.K. Harmon, D.B. Campbell, D.L. Bindschadler, J.W. Head, I.I. Shapiro, J. Geophys. Res. **91**, 385–401 (1986)
J.K. Harmon, P.J. Perillat, M.A. Slade, Icarus **149**, 1–15 (2001)
J.K. Harmon, M.A. Slade, R.A. Vélez, A. Crespo, M.J. Dryer, J.M. Johnson, Nature **369**, 213–215 (1994)
J.K. Harmon, M.A. Slade, B.J. Butler, J.W. Head, M.S. Rice, D.B. Campbell, Icarus **187**, 374–405 (2007)
S.A. Hauck, II, A.J. Dombard, R.J. Phillips, S.C. Solomon, Earth Planet. Sci. Lett. **222**, 713–728 (2004)
S.E. Hawkins, III, et al., Space Sci. Rev. (2007, this issue). doi:10.1007/s11214-007-9266-3
J.W. Head, Moon **11**, 77–99 (1974)
J.W. Head, Moon **12**, 299–329 (1975)
J.W. Head, Rev. Geophys. Space Phys. **14**, 265–300 (1976)
J.W. Head, Lunar Planet. Sci. **9**, 485–487 (1978)
J.W. Head, Earth, Moon Planets **85–86**, 153–177 (2001a)
J.W. Head, in *The Century of Space Science*, ed. by J. Bleeker, J.H. Geiss, M.C.E. Huber, A. Russo (Kluwer, The Netherlands, 2001b), pp. 1295–1323
J.W. Head, Brown University-Vernadsky Institute Microsymposium 44, abstract m44_24 (2006)
J.W. Head, A. Gifford, Moon Planets **22**, 235–258 (1980)
J.W. Head, T.B. McCord, Science **199**, 1433–1436 (1978)
J.W. Head, S.C. Solomon, Science **213**, 62–76 (1981)
J.W. Head, L. Wilson, Geophys. Res. Lett. **18**, 2121–2124 (1991)
J.W. Head, L. Wilson, Geochim. Cosmochim. Acta **55**, 2155–2175 (1992)
J.W. Head, L. Wilson, in *Workshop on Mercury: Space Environment, Surface, and Interior* (Lunar and Planetary Institute, Houston, 2001), pp. 44–45
J.W. Head, L. Wilson, M. Robinson, H. Hiesinger, C. Weitz, A. Yingst, in *Environmental Effects on Volcanic Eruptions: From Deep Oceans to Deep Space*, ed. by T. Gregg, J. Zimbelman (Plenum, New York, 2000), pp. 143–178

H. Hiesinger, J.W. Head, J. Geophys. Res. **105**, 11999–12022 (2000)
H. Hiesinger, J.W. Head, U. Wolf, R. Jaumann, G. Neukum, J. Geophys. Res. **108**, 5065 (2003). doi:10.1029/2002JE001985
N.W. Hinners, in *Apollo 16 Preliminary Science Report*. SP-315 (NASA, Washington, DC, 1972), pp. 1-1–1-3
L.L. Hood, Geophys. Res. Lett. **14**, 844–847 (1987)
G.H. Hughes, F.N. App, T.R. McGetchin, Phys. Earth Planet. Interiors **15**, 251–263 (1977)
M.A. Ivanov, J.W. Head, J. Geophys. Res. **104**, 18907–18924 (1999)
R. Jeanloz, D.L. Mitchell, A.L. Sprague, I. de Pater, Science **268**, 1455–1457 (1995)
C.L. Johnson, D.T. Sandwell, J. Geophys. Res. **97**, 13601–13610 (1992)
W.S. Kiefer, B.C. Murray, Icarus **72**, 477–491 (1987)
D.A. Kring, B.A. Cohen, J. Geophys. Res. **107**, 5009 (2002). doi:10.1029/2001JE001529
L.V. Ksanfomality, Sol. Syst. Res. **38**, 21–27 (2004)
L.V. Ksanfomality, G. Papamastorakis, N. Thomas, Planet. Space Sci. **53**, 849–859 (2005)
M.A. Leake, C.R. Chapman, S.J. Weidenschilling, D.R. Davis, R. Greenberg, Icarus **71**, 350–375 (1987)
R.P. Lin, K.A. Anderson, L.L. Hood, Icarus **74**, 529–541 (1988)
J.E. Longhi, J.E. Knittle, J.R. Holloway, H. Wanke, in *Mars*, ed. by H.H. Kiefer, B.M. Jakosky, C.W. Snyder, M.S. Matthews (University of Arizona Press, Tucson, 1992), pp. 184–208
B.K. Lucchitta et al., in *Mars*, ed. by H.H. Kiefer, B.M. Jakosky, C.W. Snyder, M.S. Matthews (University of Arizona Press, Tucson, 1992), pp. 453–492
P.G. Lucey, G.J. Taylor, E. Malaret, Science **268**, 1150–1153 (1995)
P.G. Lucey, D.T. Blewett, B.R. Hawke, J. Geophys. Res. **103**, 3679–3700 (1998)
M.C. Malin, *Proc. Lunar Planet. Science Conf. 9th*, 1978, pp. 3395–3409
A. Mallama, D. Wang, R.A. Howard, Icarus **155**, 253–264 (2002)
J.L. Margot, S.J. Peale, R.F. Jurgens, M.A. Slade, I.V. Holin, Science **316**, 710–714 (2007)
T.A. Maxwell, F. El-Baz, S.H. Ward, Geol. Soc. Am. Bull. **86**, 1273–1278 (1975)
J.F. McCauley, Phys. Earth Planet. Interiors **15**, 220–250 (1977)
J.F. McCauley, J.E. Guest, G.G. Schaber, N.J. Trask, R. Greeley, Icarus **47**, 184–202 (1981)
W.E. McClintock, M.R. Lankton, Space Sci. Rev. (2007, this issue). doi:10.1007/s11214-007-9264-5
T.B. McCord, J.B. Adams, Icarus **17**, 585–588 (1972)
T.B. McCord, R.N. Clark, J. Geophys. Res. **84**, 7664–7668 (1979)
G.E. McGill, Icarus **14**, 53–58 (1971)
G.E. McGill, Icarus **21**, 437–447 (1974)
G.E. McGill, Geophys. Res. Lett. **13**, 705–708 (1986)
G.E. McGill, E.A. King, U.S. Geol. Surv. Misc. Invest. Ser., Map I-1409 (1983)
A.F. McGuire, B.W. Hapke, Icarus **113**, 134–155 (1995)
W.B. McKinnon, in *Multi-Ring Basins*, ed. by R.O. Merrill, P.H. Schultz (Geochimica et Cosmochimica Acta, Suppl. **15**, Pergamon Press, 1981), pp. 259–273
H.J. Melosh, Icarus **31**, 221–243 (1977)
H.J. Melosh, *Proc. Lunar Planet. Science Conf. 9th*, 1978, pp. 3513–3525
H.J. Melosh, D. Dzurisin, Icarus **35**, 227–236 (1978a)
H.J. Melosh, D. Dzurisin, Icarus **33**, 141–144 (1978b)
H.J. Melosh, W.B. McKinnon, in *Mercury*, ed. by F. Vilas, C.R. Chapman, M.S. Matthews (University of Arizona Press, Tucson, 1988), pp. 374–400
M. Mendillo, J. Warell, S.S. Limaye, J. Baumgardner, A. Sprague, J.K. Wilson, Planet. Space Sci. **49**, 1501–1505 (2001)
S.M. Milkovich, J.W. Head, L. Wilson, Meteorit. Planet. Sci. **37**, 1209–1222 (2002)
H.J. Moore, C.A. Hodges, D.H. Scott, *Proc. Lunar Science Conf. 5th*, 1974, pp. 71–100
J.I. Moses, K. Rawlins, K. Zahnle, L. Dones, Icarus **137**, 197–221 (1999)
B.C. Murray, J. Geophys. Res. **80**, 2342–2344 (1975)
B.C. Murray et al., Science **185**, 169–179 (1974)
B.C. Murray, R.G. Strom, N.J. Trask, D.E. Gault, J. Geophys. Res. **80**, 2508–2514 (1975)
G. Neukum, J. Oberst, H. Hoffmann, R. Wagner, B.A. Ivanov, Planet. Space Sci. **49**, 1507–1521 (2001)
F. Nimmo, Geophys. Res. Lett. **29**, 1063 (2002). doi:10.1029/2001GL013883
F. Nimmo, T.R. Watters, Geophys. Res. Lett. **31**, L02701 (2004). doi:10.1029/2003GL018847
S.K. Noble, C.M. Pieters, Sol. Syst. Res. **37**, 31–35 (2003)
V.R. Oberbeck, Rev. Geophys. Space Phys. **13**, 337–362 (1975)
V.R. Oberbeck, R.H. Morrison, F. Hörz, W.L. Quaide, D.E. Gault, *Proc. Lunar Planet. Science Conf. 5th*, 1974, pp. 111–136
V.R. Oberbeck, W.L. Quaide, R.E. Arvidson, H.R. Aggarwal, J. Geophys. Res. **82**, 1681–1698 (1977)
B. Pavri, J.W. Head, K.B. Klose, L. Wilson, J. Geophys. Res. **97**, 13445–13478 (1992)

J.C. Pechmann, Icarus **42**, 185–210 (1980)
J.B. Pechmann, H.J. Melosh, Icarus **38**, 243–250 (1979)
R.J. Phillips, S.C. Solomon, Lunar Planet. Sci. **28**, 1107–1108 (1997)
R.J. Phillips, J.E. Conel, E.A. Abbott, W.L. Sjogren, J.B. Morton, J. Geophys. Res. **77**, 7106 (1972)
R.J. Pike, in *Mercury*, ed. by F. Vilas, C.R. Chapman, M.S. Matthews (University of Arizona Press, Tucson, 1988), pp. 165–273
R.J. Pike, P.D. Spudis, Earth, Moon Planets **39**, 129–194 (1987)
J.B. Plescia, M.P. Golombek, Geol. Soc. Am. Bull. **97**, 1289–1299 (1986)
B. Rava, B. Hapke, Icarus **71**, 397–429 (1987)
N.C. Richmond, L.L. Hood, D.L. Mitchell, R.P. Lin, M.H. Acuña, A.B. Binder, J. Geophys. Res. **110**, E05011 (2005). doi:10.1029/2005JE002405
M.S. Robinson, P.G. Lucey, Science **275**, 197–200 (1997)
M.S. Robinson, G.J. Taylor, Meteorit. Planet. Sci. **36**, 841–847 (2001)
M. Robinson, B.R. Hawke, P.G. Lucey, G.J. Taylor, P.D. Spudis, Lunar Planet. Sci. **28** (1997), abstract 1189
M. Robinson, B.R. Hawke, P.G. Lucey, G.J. Taylor, P.D. Spudis, Lunar Planet. Sci. **29** (1998), abstract 1860
G. Ryder, Eos Trans. Am. Geophys. Union **71**, 313, 322–323 (1990)
A.G. Santo et al., Planet. Space Sci. **49**, 1481–1500 (2001)
G.G. Schaber, J.F. McCauley, U.S. Geol. Surv., Map I-1199 (1980)
C.E. Schlemm, II et al., Space Sci. Rev. (2007, this issue). doi:10.1007/s11214-007-9248-5
G. Schubert, M.N. Ross, D.J. Stevenson, T. Spohn, in *Mercury*, ed. by F. Vilas, C.R. Chapman, M.S. Matthews (University of Arizona Press, Tucson, 1988), pp. 429–460
P.H. Schultz, Phys. Earth Planet. Interiors **15**, 202–219 (1977)
P.H. Schultz, in *Mercury*, ed. by F. Vilas, C.R. Chapman, M.S. Matthews (University of Arizona Press, Tucson, 1988), pp. 274–335
P.H. Schultz, D.E. Gault, Moon **12**, 159–177 (1975)
R.A. Schultz, J. Geophys. Res. **105**, 12035–12052 (2000)
D. Schulze-Makuch, J.M. Dohm, A.G. Fairén, V.R. Baker, W. Fink, R.G. Strom, Astrobiology **5**, 778–795 (2005)
V.V. Shuvalov, N.A. Artemieva, Lunar Planet. Sci. **37** (2006), abstract 1168
D.E. Smith et al., J. Geophys. Res. **106**, 23689–23722 (2001)
E.I. Smith, Icarus **28**, 543–550 (1976)
S.E. Smrekar, P. Moreels, B.J. Franklin, J. Geophys. Res. **107**, 5098 (2002). doi:10.1029/2001JE001808
V.S. Solomatov, C.C. Reese, in *Workshop on Mercury: Space Environment, Surface, and Interior* (Lunar and Planetary Institute, Houston, 2001), pp. 92–93
S.C. Solomon, Icarus **28**, 509–521 (1976)
S.C. Solomon, Phys. Earth Planet. Interiors **15**, 135–145 (1977)
S.C. Solomon, Geophys. Res. Lett. **5**, 461–464 (1978)
S.C. Solomon, Phys. Earth Planet. Interiors **19**, 168–182 (1979)
S.C. Solomon, Earth Planet. Sci. Lett. **216**, 441–455 (2003)
S.C. Solomon, J.W. Head, J. Geophys. Res. **84**, 1667–1682 (1979)
S.C. Solomon, J.W. Head, Rev. Geophys. Space Phys. **18**, 107–141 (1980)
S.C. Solomon et al., J. Geophys. Res. **97**, 13199–13256 (1992)
S.C. Solomon et al., Science **307**, 1214–1220 (2005)
A.L. Sprague, R.W.H. Kozlowski, F.C. Witteborn, D.P. Cruikshank, D.H. Wooden, Icarus **109**, 156–167 (1994)
A.L. Sprague, D.M. Hunten, K. Lodders, Icarus **118**, 211–215 (1995)
A.L. Sprague, W.J. Schmitt, R.E. Hill, Icarus **135**, 60–68 (1998)
A.L. Sprague, J.P. Emery, K.L. Donaldson, R.W. Russell, D.K. Lynch, A.L. Mazuk, Meteorit. Planet. Sci. **37**, 1255–1268 (2002)
P.D. Spudis, in Repts. Planet. Geol. Prog. (NASA TM-87563, 1985), pp. 595–597
P.D. Spudis, J.E. Guest, in *Mercury*, ed. by F. Vilas, C.R. Chapman, M.S. Matthews (University of Arizona Press, Tucson, 1988), pp. 118–164
P.D. Spudis, B.R. Hawke, in *Workshop on the Geology and Petrology of the Apollo 15 Landing Site*. LPI Tech. Rept. 86-03 (Lunar and Planetary Institute, Houston, TX, 1986), pp. 105–107
P.D. Spudis, J.G. Prosser, U.S. Geol. Surv., Map I-1659 (1984)
D.K. Srinivasan, M.E. Perry, K.B. Fielhauer, D.E. Smith, M.T. Zuber, Space Sci. Rev. (2007, this issue). doi:10.1007/s11214-007-9270-7
S. Stanley, J. Bloxham, W.E. Hutchison, M.T. Zuber, Earth Planet. Sci. Lett. **234**, 27–38 (2005)
L. Starukhina, J. Geophys. Res. **106**, 14701–14710 (2001)
D.J. Stevenson, Science **287**, 997–1005 (2000)

E.R. Stofan, V.E. Hamilton, D.M. Janes, S.E. Smrekar, in *Venus II*, ed. by S.W. Brougher, D.M. Hunten, R.J. Phillips (University of Arizona Press, Tucson, 1997), pp. 931–965
R.G. Strom, Mod. Geol. **2**, 133–157 (1972)
R.G. Strom, Phys. Earth Planet. Interiors **15**, 156–172 (1977)
R.G. Strom, *Mercury: The Elusive Planet* (Smithsonian Inst. Press, Washington, 1987), 197 pp
R.G. Strom, G. Neukum, in *Mercury*, ed. by F. Vilas, C.R. Chapman, M.S. Matthews (University of Arizona Press, Tucson, 1988), pp. 336–373
R.G. Strom, A.L. Sprague, *Exploring Mercury: The Iron Planet* (Springer, New York, 2003), 216 pp
R.G. Strom, N.J. Trask, J.E. Guest, J. Geophys. Res. **80**, 2478–2507 (1975)
R.G. Strom, S.K. Croft, N.G. Barlow, in *Mars*, ed. by H.H. Kiefer, B.M. Jakosky, C.W. Snyder, M.S. Matthews (University of Arizona Press, Tucson, 1992), pp. 383–423
R.G. Strom, R. Malhotra, T. Ito, F. Yoshida, D.A. Kring, Science **309**, 1847–1850 (2005)
D.E. Stuart-Alexander, U.S. Geol. Surv., Misc. Invest. Ser., Map I-1047 (1978)
F. Tera, D.A. Papanastassiou, G.J. Wasserburg, Earth Planet. Sci. Lett. **22**, 1–21 (1974)
P.G. Thomas, P. Masson, L. Fleitout, in *Mercury*, ed. by F. Vilas, C.R. Chapman, M.S. Matthews (University of Arizona Press, Tucson, 1988), pp. 401–428
S. Tompkins, C.M. Pieters, Meteorit. Planet. Sci. **34**, 25–41 (1999)
N.J. Trask, D. Dzurisin, U.S. Geol. Surv. Misc. Invest. Ser., Map I-1658 (1984)
N.J. Trask, J.E. Guest, J. Geophys. Res. **80**, 2461–2477 (1975)
N.J. Trask, J.F. McCauley, Earth Planet. Sci. Lett. **14**, 201–206 (1972)
N.J. Trask, R.G. Strom, Icarus **28**, 559–563 (1976)
A.L. Tyler, R.W.H. Kozlowski, L.A. Lebofsky, Geophys. Res. Lett. **15**, 808–811 (1988)
A.R. Vasavada, D.A. Paige, S.E. Wood, Icarus **141**, 179–193 (1999)
J. Veverka, P. Helfenstein, B. Hapke, J.D. Goguen, in *Mercury*, ed. by F. Vilas, C.R. Chapman, M.S. Matthews (University of Arizona Press, Tucson, 1988), pp. 37–58
F. Vilas, Icarus **64**, 133–138 (1985)
F. Vilas, in *Mercury*, ed. by F. Vilas, C.R. Chapman, M.S. Matthews (University of Arizona Press, Tucson, 1988), pp. 59–76
F. Vilas, T.B. McCord, Icarus **28**, 593–599 (1976)
F. Vilas, M.A. Leake, W.W. Mendell, Icarus **59**, 60–68 (1984)
F. Vilas, P.S. Cobian, N.G. Barlow, S.M. Lederer, Planet. Space Sci. **53**, 1496–1500 (2005)
D. Vokrouhlicky, P. Farinella, W.F. Bottke Jr., Icarus **148**, 147 (2000)
J. Warell, Icarus **156**, 303–317 (2002)
J. Warell, Icarus **167**, 271–286 (2004)
J. Warell, D.T. Blewett, Icarus **168**, 257–276 (2004)
J. Warell, S.S. Limaye, Planet. Space Sci. **49**, 1531–1552 (2001)
J. Warell, A.L. Sprague, J.P. Emery, R.W.H. Kozlowski, A. Long, Icarus **180**, 281–291 (2006)
T.R. Watters, J. Geophys. Res. **93**, 10236–10254 (1988)
T.R. Watters, J. Geophys. Res. **96**, 15599–15616 (1991)
T.R. Watters, J. Geophys. Res. **98**, 17049–17060 (1993)
T.R. Watters, J. Geophys. Res. **108**, 5054 (2003). doi:10.1029/2002JE0001934
T.R. Watters, Icarus **171**, 284–294 (2004)
T.R. Watters, M.S. Robinson, A.C. Cook, Geology **26**, 991–994 (1998)
T.R. Watters, A.C. Cook, M.S. Robinson, Planet. Space Sci. **49**, 1523–1530 (2001)
T.R. Watters, R.A. Schultz, M.S. Robinson, A.C. Cook, Geophys. Res. Lett. **29**, 1542 (2002). doi:10.1029/2001GL014308
T.R. Watters, M.S. Robinson, C.R. Bina, P.D. Spudis, Geophys. Res. Lett. **31**, L04701 (2004). doi:10.1029/2003GL019171
T.R. Watters, F. Nimmo, M.S. Robinson, Geology **33**, 669–672 (2005)
M.A. Wieczorek, M.T. Zuber, J. Geophys. Res. **106**, 27853–27864 (2001)
D.E. Wilhelms, Icarus **28**, 551–558 (1976a)
D.E. Wilhelms, *Proc. Lunar Planet. Science Conf. 7th*, 1976b, pp. 2883–2901
D.E. Wilhelms, *The Geologic History of the Moon*. Prof. Paper 1348 (U.S. Geological Survey Washington, DC, 1987), 302 pp
D.E. Wilhelms, F. El-Baz, U.S. Geol. Surv. Misc. Geol. Invest. Ser., Map I-948 (1977)
D.E. Wilhelms, J. McCauley, U.S. Geol. Surv. Misc. Inv. Ser., Map I-703 (1971)
C.A. Wood, J.W. Head, *Proc. Lunar Planet. Science Conf. 7th*, 1976, pp. 3629–3651
J.W. Young, T.K. Mattingly, C.M. Duke, in Apollo 16 Preliminary Science Report, SP-315 (NASA, Washington, DC, 1972) pp. 5-1–5-6
M.T. Zuber et al., Space Sci. Rev. (2007, this issue). doi:10.1007/s11214-007-9265-4